UNIVERSITÀ
DI PAVIA

UNIVERSITY OF PAVIA

FACULTY OF ENGINEERING

DEPARTMENT OF INDUSTRIAL AND INFORMATION ENGINEERING

MASTER'S DEGREE IN BIOENGINEERING

MASTER THESIS

Assessing the impact of filtering on BOLD signal extraction within the Dynamic Causal Modelling pipeline: Implications for the effective connectivity of a visuomotor task

Valutazione dell'impatto del filtraggio sull'estrazione del segnale BOLD nella pipeline del Dynamic Causal Modelling: Implicazioni sulla connettività effettiva in un compito visuomotorio

Candidate: Protopop Maria

Supervisor: Prof. Gandini Claudia

Co-supervisors:

Dr. Lorenzi Roberta Maria

Dr. Korkmaz Gökçe

A.Y. 2024/2025

Abstract

Functional Magnetic Resonance Imaging (fMRI) is a non-invasive neuroimaging technique that measures brain activity by detecting changes in blood oxygenation and flow, which are linked to neural activity. This indirect measure is captured by the Blood Oxygenation Level Dependent (BOLD) signal. While fMRI data are commonly analysed to identify which brain regions are active during a task, understanding how these regions influence each other, known as effective connectivity, requires a more advanced modelling approach. Dynamic Causal Modelling (DCM) is a computational framework that estimates the directional, causal interactions between brain regions, allowing researchers to infer how activity in one region affects activity in another. Temporal filtering is a common preprocessing step in fMRI analyses, aimed to isolate physiologically relevant frequency components of the BOLD signal and reduce spectral components that represent physiological noise (e.g., cardiac and respiratory). However, its impact on downstream analyses, particularly within the DCM framework of causal connectivity estimation, is not fully explored.

This study investigates the effects of bandpass filtering (0.008–0.09 Hz) on BOLD signal characteristics and on DCM within a previously defined visuomotor network. The visuomotor network under analysis, as well as the experimental protocol, were adopted from previous studies on the same dataset. The analysis was conducted on a cohort of 21 healthy subjects performing a power grip task and guided by a visual cue. The network included six volumes of interest (VOIs): bilateral primary visual cortex, left primary motor cortex, left supplementary motor area, left premotor cortex, left cingulate cortex, left superior parietal lobule, and right cerebellar lobule VI.

For a first assessment of the bandpass filter on known reference, synthetic signals were generated and compared through the analysis of the power spectral density (PSD). PSD analyses were extended to the experimental data where three preprocessing conditions were compared: no filtering, filtering applied before VOI extraction, and filtering applied after VOI extraction. Results from synthetic and experimental data showed that temporal filtering alters the spectral and temporal properties of the BOLD signal, reducing signal variance and amplitude within the passband. When applied before VOI extraction, filtering also affected the statistical detection of regional activations, leading to reduced activation extent and

incomplete VOI definition in a subset of subjects. In contrast, filtering applied after VOI extraction preserved signal characteristics more effectively.

For each of the three filtering conditions different DCM models, representing different hypotheses of effective connectivity within the visuomotor network, were specified and estimated. Group-level analysis was implemented using Random-Effects Bayesian Model Selection (RFX-BMS) evaluating competing models across subjects to identify the winning (i.e., most likely) model describing fixed connectivity patterns in the network. Once the winning model was selected, Bayesian Model Averaging (BMA) was applied to combine parameter estimates across subjects and obtain a representative group model for each filtering condition. Despite these signal-level differences, model comparison results were consistent across preprocessing conditions, identifying the same network architecture as the optimal model. This model highlighted a visuo-to-plan loop driven by the primary visual cortex with the primary motor cortex linking planning and execution. Filtering application both before and after highlighted a slight increase in the visual-to-plan connections, while reducing planning to motor connections. However, effective connectivity estimates did not show widespread variations across conditions and only limited significant differences. These findings suggest that while temporal filtering significantly affects the BOLD signal and the definition of volumes of interest, its impact on the fixed effective connectivity estimation is limited. The results highlight the importance of considering the position of filtering within the preprocessing pipeline, particularly with respect to VOI extraction, and support the relative robustness of DCM to spectral changes due to filtering.

Sommario

La risonanza magnetica funzionale (fMRI) è una tecnica di neuroimaging non invasiva che consente di misurare l'attività cerebrale attraverso la rilevazione delle variazioni nell'ossigenazione e nel flusso sanguigno. La misura è indiretta ed è rappresentata dal segnale BOLD (Blood Oxygenation Level Dependent). Sebbene i dati fMRI siano analizzati comunemente per identificare le regioni cerebrali attive, la comprensione dell'interazione tra le regioni, nota come connettività efficace, richiede approcci di modellazione più avanzati. Il Dynamic Causal Modelling (DCM) è un framework computazionale che permette di stimare le interazioni causali e direzionali tra regioni cerebrali, permettendo di stimare come l'attività di una regione influenzi quella di un'altra. Un passaggio rilevante all'interno della pipeline di analisi DCM e del preprocessing dei dati fMRI è costituito dal filtraggio temporale, in quanto influenza i segnali su cui si basa la stima della connettività efficace. Esso è finalizzato a ridurre le frequenze del segnale associate a rumore fisiologico (ad esempio attività cardiaca e respiratoria) e isolare le componenti in frequenza fisiologicamente rilevanti del segnale BOLD. Tuttavia, il suo impatto sulle analisi successive, in particolare nell'ambito della stima della connettività causale tramite DCM, non è ancora completamente esplorato.

Questo studio indaga gli effetti del filtraggio passa-banda (0.008-0.09 Hz) sulle caratteristiche del segnale BOLD e sulle stime DCM all'interno di una rete visuomotoria. La rete visuomotoria analizzata, così come il protocollo sperimentale, sono stati adottati da studi precedenti sullo stesso dataset. L'analisi è stata condotta su un campione di 21 soggetti sani impegnati in un compito di presa di forza guidato da uno stimolo visivo. La rete considerata include sei volumi di interesse (VOI): la corteccia visiva primaria bilaterale, corteccia premotoria sinistra, area motoria supplementare e corteccia premotoria sinistra, corteccia cingolata sinistra, lobulo parietale superiore sinistro e cervelletto destro (lobulo VI).

Per una prima valutazione degli effetti del filtraggio, sono stati generati segnali sintetici, con componenti in frequenza note, e confrontati mediante l'analisi della densità spettrale di potenza (PSD). L'analisi PSD è stata estesa ai dati sperimentali, confrontando tre diverse condizioni di preprocessing: assenza di filtraggio, filtraggio applicato prima dell'estrazione delle VOI, filtraggio applicato dopo l'estrazione delle VOI. I risultati, sia su dati sintetici che sperimentali, hanno mostrato che il filtraggio modifica le proprietà spettrali e temporali del

segnale BOLD, riducendo ampiezza e varianza in banda passante. Quando applicato prima dell'estrazione delle VOI, il filtraggio ha influenzato la rilevazione statistica delle attivazioni regionali, determinando una riduzione dell'estensione delle attivazioni e definizione incompleta delle VOI in un sottoinsieme di soggetti. Quando applicato dopo l'estrazione delle VOI, ha preservato invece in maniera più efficace le caratteristiche del segnale.

Per ciascuna delle tre condizioni di filtraggio, sono stati stimati diversi modelli DCM, che rappresentano diverse ipotesi di connettività efficace all'interno della rete visuomotoria. L'analisi a livello di gruppo è stata condotta tramite Random-Effects Bayesian Model Selection (RFX-BMS) per identificare il modello più probabile tra quelli definiti. Una volta selezionato il modello più probabile, è stata applicata la Bayesian Model Averaging (BMA) per combinare le stime dei parametri tra i soggetti, ottenendo un modello rappresentativo a livello di gruppo per ciascuna condizione di filtraggio. Nonostante le differenze osservate a livello di segnale, il modello di rete ottimale è risultato lo stesso per tutte e tre le condizioni di filtraggio. Tale modello evidenzia un circuito visuo-motorio guidato dalla corteccia visiva primaria, con la corteccia motoria primaria a svolgere un ruolo di collegamento tra pianificazione ed esecuzione. L'applicazione del filtraggio, sia prima che dopo l'estrazione delle VOI, ha evidenziato un lieve aumento delle connessioni tra corteccia visiva primaria e aree coinvolte nella pianificazione motoria, e una riduzione delle connessioni tra pianificazione e area motoria. Tuttavia, le stime di connettività efficace non hanno mostrato variazioni diffuse tra le condizioni con un numero limitato di differenze significative tra le connessioni. Questi risultati suggeriscono che sebbene il filtraggio influenzi il segnale BOLD e la definizione dei volumi di interesse, il suo impatto sulla stima della connettività efficace fissa risulta più ridotto. Lo studio evidenza l'importanza di considerare la posizione del filtraggio all'interno della pipeline di preprocessing, in particolare rispetto all'estrazione delle VOI, e supporta la relativa robustezza del DCM rispetto alle variazioni spettrali introdotto dal filtro.

Index

1. Principles of Magnetic Resonance Imaging

Magnetic Resonance Imaging (MRI) is an imaging technique widely used in clinical practice and research. MRI provides excellent soft tissue contrast with high spatial resolution, enabling the acquisition of three-dimensional tomographic images and the investigation of dynamic physiological processes through appropriate acquisition strategies. Therefore, it represents a powerful medical investigation tool due to its sensitivity to differences in tissue properties, allowing the acquisition of both anatomical and functional information (Brown et al., 2014). Moreover, MRI is a non-invasive imaging modality, as it does not rely on ionizing radiation, thus allowing repeated scans under defined technical constraints (Plewes & Kucharczyk, 2012).

From a physical perspective, MRI is based on the application of Nuclear Magnetic Resonance (NMR) principles, a phenomenon that was first described experimentally by Bloch and Purcell in 1946, for which they were both awarded the Nobel Prize for Physics in 1952 (Grover et al., 2015). The term 'magnetic' refers to the use of strong static and time-varying magnetic fields, while 'resonance' refers to the condition in which the radiofrequency of a time-varying magnetic field applied matches the precessional frequency of nuclear spins within the biological tissue, that subsequently re-emit electromagnetic radiation at the same frequency (Brown et al., 2014). These concepts will be thoroughly described in the following section.

1.1 MRI Physics Fundamentals

MRI exploits the magnetic properties of nuclei with non-zero spin and electric charge in the presence of external magnetic fields. The nuclei primarily involved in image formation are hydrogen nuclei (^{1}H), due to the high concentration in biological tissues particularly in the form of water (Plewes & Kucharczyk, 2012). An individual hydrogen nucleus is a single positively charged proton.

Spin is an intrinsic form of angular momentum possessed by quantum particles, such as atomic nuclei. It is important to emphasize that nuclear spin is not to be interpreted as a classical rotation of the particle, but as an intrinsic quantum mechanical property.

Nevertheless, for the functional understanding of the principles of MRI, analogies based on Newtonian physics can be employed (Plewes & Kucharczyk, 2012).

The magnetic property of the proton is given by its intrinsic angular momentum (spin) and its electric charge, leading to the classical analogy of the proton behaving like a bar magnet or a magnetic dipole. This magnetic property is described by the magnetic moment $\vec{\mu}$, which is proportional to the intrinsic angular momentum $\vec{P}$ through the gyromagnetic ratio[1] γ, a constant specific for each nuclear species:

$$\vec{\mu} = \gamma \vec{P} \tag{1}$$

To exploit the magnetic properties of the nuclear spin (Figure 1.b) an external static magnetic field is required. In MRI this field is referred to as $\vec{B}_{0,}$ is characterized by constant direction and magnitude. It is conventionally aligned with the z-axis, which is referred to as the longitudinal direction. In clinical MRI scanners B_0 strength typically ranges between 1.5T and 3T and is generated by a superconducting magnet to ensure a highly homogenous field.

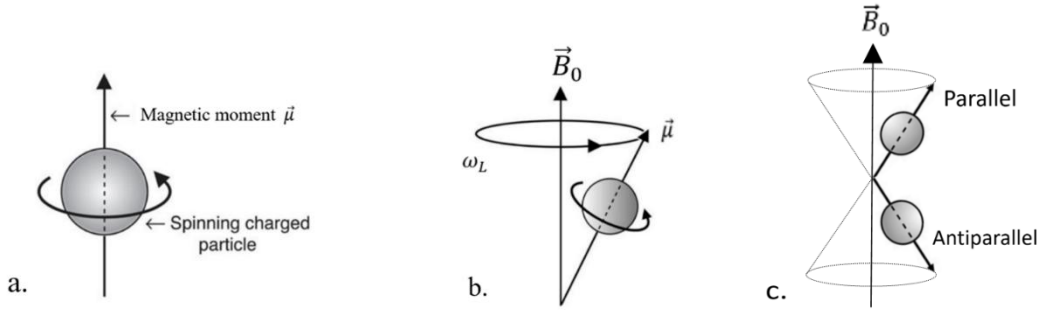

Figure 1. a) In the absence of an external magnetic field, a proton rotating about its own axis generates a magnetic moment $\vec{\mu}$ b) In the presence of an external static magnetic field $\vec{B}_{0,}$ a proton not only spins about its axis but processes about the axis $\vec{B}_0$ at the Larmor frequency ω_L c) In the presence of $\vec{B}_0$ protons split in two energy levels, aligning parallel and antiparallel orientation relative to $\vec{B}_0$ (Adapted from Ray H. Hashemi, 2018)

When $\vec{B}_0$ is applied, the magnetic moment $\vec{\mu}$ associated to the nuclear spin is subjected to a torque that causes it to undergo a precessional motion around the field axis (Figure 1.b) analogous to the behaviour of a magnetic dipole with angular momentum in a static field.

[1] For the proton $\gamma = 2.675 \times 10^8\ rad/\text{s/T}$ or $\gamma = 42.58\ MHz/T$

The angular frequency of this precessional motion is known as the Larmor frequency ω_L (expressed in rad/s) is described in the Larmor Equation:

$$\omega_L = \gamma B_0 \quad (2)$$

In the equation (2), γ is the gyromagnetic ratio, B_0 is the static magnetic field strength.

Application of a strong external magnetic field (B_0) aligns the proton spins either parallel or antiparallel to the external field as shown in Figure 1.c, and this is explained by the allowed spin states of the proton. The number of allowed spin states is determined in relation to the spin quantum number I, which is quantized and can only assume integer or half-integer values. These spin states are labelled by the magnetic quantum number m and can assume $2I + 1$ values:

$$m = -I, -I + 1, \ldots, I - 1, I \quad (3)$$

In the presence of a magnetic field, spin states that correspond to different m values are split into discrete energy levels, a phenomenon known as Zeeman effect (Cheng & Haacke, 2001).

For ^{1}H spin quantum number is $I = 1/2$, resulting in two possible energy states, corresponding to $m = +1/2$ and $m = -1/2$. When $\vec{B}_0$ field is applied, proton spins distribute between the two discrete energy state, a low energy state ($m = +1/2$) and a high energy state ($m = -1/2$), which correspond respectively to parallel and antiparallel orientations relative to the field direction.

In a system containing many nuclear spins placed in a static magnetic field, the total contribution of the magnetic moments is the net magnetization $\vec{M}$, defined as the vector sum of all magnetic moments per unit volume:

$$\vec{M} = \frac{1}{V}\sum_i \vec{\mu}_i \quad (4)$$

where V is the volume subjected to a constant static magnetic field, and μ_i is the magnetic moment of the i-th nucleus.

In the absence of an external field, nuclear magnetic moments $\vec{\mu}_i$ would be randomly oriented, resulting in a null net magnetization $\vec{M}$. In the presence of the static there is a net excess of spins that occupy the low energy state. This results in a net magnetization vector

$\vec{M}_0$ oriented along the $\vec{B}_0$ axis, given that the transverse components cancel each other out due to random phase distribution. Magnetization represents the measurable physical quantity in MRI, as a time-varying magnetization generates a magnetic flux through the receiver coil, inducing an electromotive force according to Faraday's law. However, being $\vec{M}_0$ time invariant and aligned with the strong static magnetic field $\vec{B}_0$, it does not generate a detectable MR signal (Brown et al., 2014).

To generate a detectable MR signal, the net magnetization must be tipped away from the direction of $\vec{B}_0$, so that the magnetization vector M_0 is rotated in the transverse plane x-y and is free to precess around the z-axis. This is achieved by applying for a short time duration an alternating magnetic field, generally denoted as $B_1(t)$, which is perpendicular to $\vec{B}_0$, and must have a frequency equal to the Larmor Frequency of the nucleus. This is the resonance condition in MRI (Plewes & Kucharczyk, 2012). As Larmor Frequencies are in the radiofrequency range of the electromagnetic spectrum, these alternating magnetic fields are referred to as radiofrequency (RF) pulses. In MRI this frequencies range between tens to hundreds MHz (Ray H. Hashemi et al., 2018). As energy is absorbed from the RF pulse, the net magnetization rotates away from the longitudinal direction. The amount of rotation, denoted as the flip angle, depends on the strength and duration of the RF pulse (Pooley, 2005). In this explicative case the flip angle has a value of 90°. Only the transverse component $\vec{M}_{xy}$ of the magnetization contributes to signal formation, as it precesses around the z-axis, therefore varies in time at the Larmor frequency, and is not aligned with the strong $\vec{B}_0$. This time-varying $\vec{M}_{xy}$ induces a voltage in a receiver coil, generating a detectable MR signal.

1.2 Relaxation times

Following the RF excitation, nuclear spins gradually dissipate the energy acquired through the RF pulse and return towards thermal equilibrium. At the same time, spins progressively lose their phase coherence due to interactions within the spin system. As a result, the net magnetization that has been flipped into the transverse plane returns to its equilibrium alignment along the direction of the static magnetic field $\vec{B}_0$. This describes the relaxation process that occurs after the RF pulse is turned off, resulting in the change of magnitude and orientation of the net magnetization vector (Ray H. Hashemi et al., 2018).

There are two relaxation processes that begin simultaneously involving the recovery of the longitudinal magnetization M_z, and the decay of the transversal magnetization M_{xy}. These mechanisms are known as longitudinal relaxation and transverse relaxation, respectively described by T1 and T2 time constants (Brown et al., 2014; Grover et al., 2015). The return to equilibrium of the net magnetization vector is analytically described by the Bloch equations:

$$\frac{dM_z(t)}{dt} = \gamma\left(\vec{M}(t) \times \vec{B}_0\right)_z - \frac{M_0 - M_z(t)}{T1} \tag{5}$$

$$\frac{dM_{xy}(t)}{dt} = \gamma\left(\vec{M}(t) \times \vec{B}_0\right)_{xy} + \frac{M_{xy}(t)}{T_2}$$

Their solutions describe the exponential recovery of longitudinal magnetization (6) and exponential decay of transverse magnetization (7).

Time constants T1 and T2 are inherent tissue properties, therefore different tissues have different rates of relaxation at a given B_0 strength, as shown in Table 1.

Table 1. Rough Values for the Time Constants T1 and T2 at Field Strength of 1.5 T (Huettel, 2014)

	Gray Matter	White Matter	Cerebrospinal Fluid
T1	900 ms	600 ms	>2000 ms
T2	100 ms	80 ms	2000 ms

This provides the flexibility of MRI in defining imaging contrast, by suitably 'weighting' these properties. This aspect will be discussed in the contrast mechanisms chapter.

1.2.1 Longitudinal Relaxation (T1)

Longitudinal relaxation, also called spin-lattice relaxation, is caused by the energy exchange between spins and the surrounding molecular environment and describes the recovery of the longitudinal magnetization $M_z(t)$ to its equilibrium value M_0 along the z-axis (Ray H. Hashemi et al., 2018b). The longitudinal magnetization $M_z(t)$ displays an exponential evolution in time (Figure 2) described by the following expression:

$$M_z(t) = M_0(1 - e^{-\frac{t}{T1}}) \tag{6}$$

where M0 is the equilibrium magnetization and T1 is the time constant at which ~63.2 % of the longitudinal magnetization has recovered.

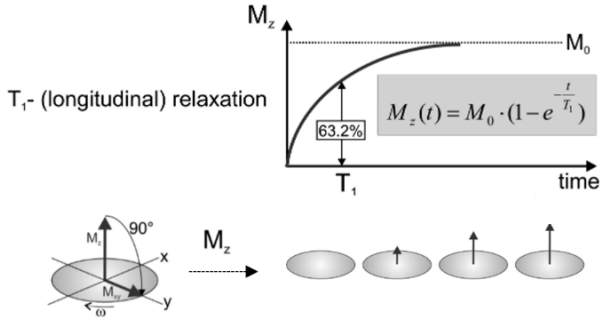

Figure 2. Exponential recovery of the longitudinal magnetization to equilibrium, characterized by the T1 time constant, following a 90° excitation pulse (Adapted from Jung & Weigel, 2013).

1.2.2 Transverse Relaxation (T2)

Transverse relaxation, or spin-spin relaxation, describes the decay of the transverse magnetization M_{xy} (Figure 3), caused by a gradual loss of phase coherence between spins due to interactions within the spins system. As neighbouring spins affect each other's magnetic fields locally, leading to a different precessional frequency that contributes to the dephasing of spins:

$$M_{xy}(t) = M_{xy}(0)e^{-\frac{t}{T2}} \tag{7}$$

In the equation T2 is the time constant corresponding to the time that it takes $M_{xy}(0)$ to decay to ~37% of its initial value.

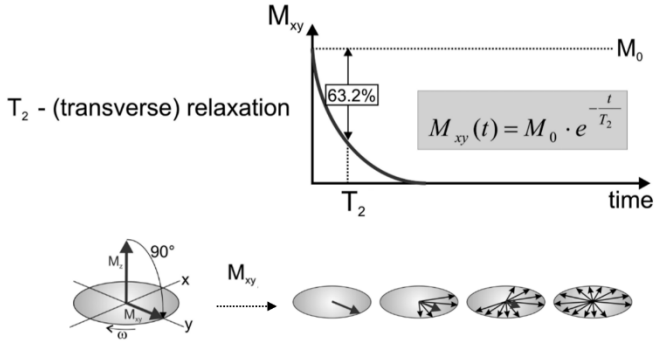

Figure 3. Exponential decay of the transverse magnetization to equilibrium, characterized by the T2 time constant, following a 90° excitation pulse (Adapted from Jung & Weigel, 2013).

1.2.3 T2* Relaxation and Free Induction Decay

It is important to note that in practice the static magnetic field B_0 is not perfectly homogeneous, due to imperfections in the magnet producing it and magnetic susceptibility differences in biological tissues. As a result, spins experience slightly different local magnetic fields and precess at different Larmor frequencies, thus contributing to spin dephasing(Plewes & Kucharczyk, 2012). Therefore, transverse relaxation includes the dephasing due to the spin-spin interaction described by the T2 time constant, and dephasing caused by field inhomogeneities described by T2'. The combined effects result in the transverse relaxation described by T2* time constant, expressed as:

$$\frac{1}{T2^*} = \frac{1}{T2} + \frac{1}{T2'} \tag{8}$$

Following the RF pulse, the observable signal is the free induction decay (FID) signal. It is an oscillating and exponentially decaying signal that reflects the decay of the transverse magnetization $M_{xy}(t)$. Given the presence of inevitable field inhomogeneities, the decay is governed by the T2* time constant, which leads to a more rapid signal loss compared to the T2 relaxation. The dephasing caused by field inhomogeneities can be reversed by applying a 180° refocusing pulse after the initial 90° excitation pulse, generating an echo signal. This pulse sequence is referred to as spin-echo, one of the fundamental pulse sequences in MRI (Figure 4).

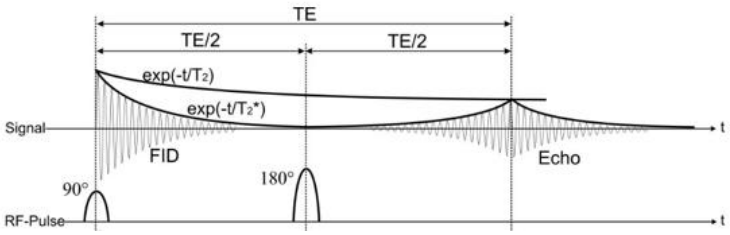

Figure 4. The Spin Echo sequence consists of a 90° excitation pulse and a 180° refocusing pulse. All spin isochromats (i.e., spins at the same Larmor frequency) are fully rephased at TE, (Adapted from Jung & Weigel, 2013)

1.3 Image Reconstruction - Spatial Encoding

To form MR images, the measured signal must be correlated with the spatial location of its sources. Since the MR signal originates from the entire spin system within the uniform B_0 field, spatial localization would not be possible without additional encoding mechanisms. Spatial encoding is achieved through the application of spatially linearly varying magnetic fields, known as gradient fields. When a gradient field is applied along a certain direction, spins located at different positions experience different magnetic field strengths and precess at different Larmor frequencies (Brown et al., 2014; Plewes & Kucharczyk, 2012). This relationship follows the Larmor equation (*2*):

$$\omega(x) = \gamma B(x) = \gamma(B_0 - G_z \cdot x) \tag{9}$$

Where x is the spatial coordinate in the direction of the gradient field, and $B(x)$ describes the linear variations of the magnetic field. Therefore, application of a gradient changes the strength of the static magnetic field a given spatial location.

By sequentially applying gradients along the three orthogonal directions (x, y and z), spatial information is encoded in the frequency and phase of the MR signal, enabling image reconstruction through inverse Fourier transformation. Magnetic field gradients are usually denoted as G_z, G_y and G_x, and respectively enable slice selection, phase encoding and frequency encoding. The encoding role of the gradients depends on the direction and timing of their application. The slice selection gradient G_z, is applied along the z direction simultaneously with the RF pulse. As the gradient G_z causes the Larmor frequency to vary along the z axis, only spins whose resonance frequency is within the bandwidth of the RF

pulse are exited, allowing to excite a slice on the xy plane. Phase encoding gradient G_y is applied after slice selection along the y axis for a brief period. This causes spins to have different frequencies in the y direction that result in a phase shift proportional to their spatial position. Spins maintain the phase difference after the gradient is turned off. By varying the amplitude of G_y across successive repetitions, different offsets for the phase are introduced, allowing to encode spatial information along direction y. Lastly, frequency encoding or G_x, also referred to as readout gradient is applied while data is acquired. This causes spins along the x direction to precess at different Larmor Frequencies, allowing spatial encoding in this direction. The signal is meanwhile measured by a receiver coil, constituting one redout.

The acquired data, sampled from the receiver coil, is stored in a matrix called k-space, which stores the spatial frequency information. Data acquired during one readout period constitutes one line in the k-space. Successive repetitions of a pulse sequence with different G_y amplitudes allow to fill additional lines in the matrix(Val M. Runge et al., 2018). The central region of k-space contains low spatial frequencies that determine the coarse structure of the objects referred to as the contrast of the image. While the boarders of the k-space contain higher spatial frequencies that encode contours and borders in the image (Moratal et al., 2008).

1.4 Pulse Sequences

Magnetic resonance experiments are all defined by the pulse sequences used to control the timing and amplitude of the RF pulses and magnetic field gradients. A pulse sequence is schematically represented by a sequence diagram as shown in Figure 5 which illustrates the temporal sequence between RF pulses, gradient fields, and data acquisition events.

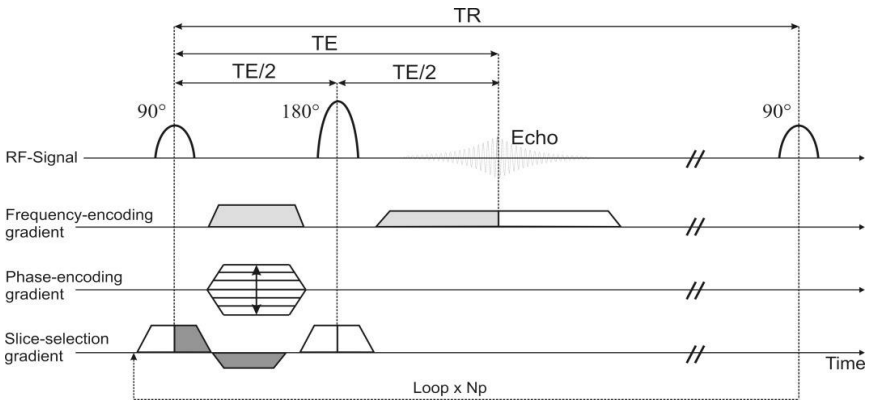

Figure 5. The spin echo sequence with all RF-pulses and magnetic field gradients for the spatial encoding. The sequence is repeated Np times in the phase-encoding direction (Jung & Weigel, 2013).

By controlling the parameters that define a pulse sequence, key aspects of an MR experiment are determined, such as how magnetization evolves, and how spatial encoding and contrast are created (John P. Mugler, 1999). Among these parameters, the most important are the repetition time (TR) and echo time (TE). TR is defined as the time interval between two subsequent excitation pulses. TE is the time between excitation and data acquisition. These parameters are controlled by an operator, unlike T1 and T2, which are inherent tissue properties (Ray H. Hashemi, 2018). Fundamental pulse sequences used are the Spin-Echo (SE) and Gradient Echo (GE) also called Gradient Recalled Echo (GRE) sequences.

As already mentioned, in the SE sequence the 90° pulse is followed by a 180° refocusing pulse forming an echo at TE, the sequence is repeated every TR (Figure 5). GRE sequences do not use the 180° refocusing pulse but only uses gradients to generate the signal echo. Following a 90° excitation pulse, the detectable MR signal at the TE can be expressed as:

$$M_{xy}(t) = M_0\left(1 - e^{-\frac{TR}{T1}}\right)e^{-\frac{TE}{T2}} \quad (10)$$

Where M_0 is the equilibrium magnetization, proportional to proton density. This equation provides the foundation for manipulating the signal from a particular tissue by controlling TR and TE. In fact, contrast is defined as the difference of signal intensities for different tissues, and the choice of timing parameters can be used to generate images with contrast reflecting different relaxation mechanisms in different tissues. The main contrast generating mechanisms are based on proton density, T1, T2 and T2* relaxations.

Proton density images provide contrast based on the number of protons present within each voxel that contribute to the net magnetization of the respective voxel. The proton density differs in different tissue types. To maximize proton density contrast, pulse sequences with long TR (e.g., two or three times greater than T1), and short TE (e.g., one tenth as long of the T2), are used. For a T1 contrast, pulse sequences must have short TE and intermediate TR. For the T2 contrast, long TR and intermediate TE. Proton density, T1 and T2 weighted images are shown in Figure 6.

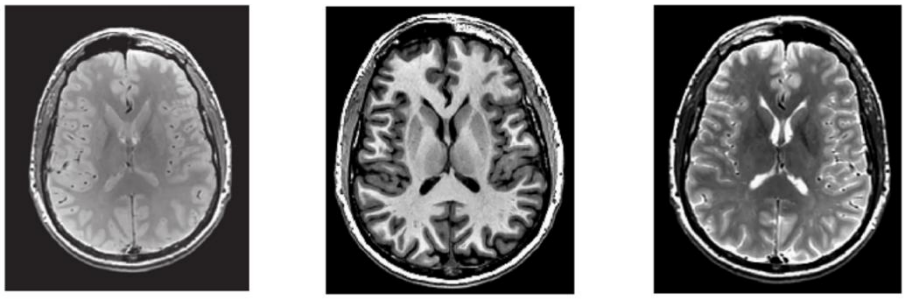

a. b. c.

Figure 6. a) Proton Density weighted b) T1 weighted c) T2 weighted images (Adapted from Jung & Weigel, 2013)

2. Functional Magnetic Resonance Imaging

Functional Magnetic Resonance Imaging (fMRI) is used to map the brain activity over time. The first successful experiments were conducted by Dr. John Belliveau and his colleagues at the Massachusetts General Hospital in 1991, in which the images were acquired sequentially by using a technique called Echo Planar Imaging (EPI). This acquisition technique allows rapid acquisitions at approximately the same rate as the physiological changes of interest ($\sim 100\, ms/slice$)(Huettel et al., 2014). In the initial approach to fMRI, two sequential injections of Gadolinium were administrated during the data acquisition, to generate maps of cerebral blood volume before and during visual stimulation. The subtraction of the resting map and the active revealed a localized increase in the blood volume in the visual cortex. In the same year, the first successful fMRI using endogenous Blood Oxygenation Level Dependent (BOLD) contrast were obtained independently by research groups led by Kenneth Kwong at the Massachusetts General Hospital and Seiji Ogawa at the University of Minnesota. This methodology did not require exogenous contrast, but exploited the magnetic susceptibility given by variations in haemoglobin oxygenation. Thus, fMRI allows to measure the BOLD signal, which provides an indirect measure of neuronal activity reflected by the hemodynamic response and this revolutionized neuroscience studies (Bandettini, 2012; Gregory Ashby, 2015).

2.1 Physiological basis of the BOLD signal

To understand the contrast mechanism used in BOLD fMRI, it is necessary to understand the underlying physiological processes that link neural activity to variations in blood oxygenation. When a region of the brain is activated during a cognitive or motor task, the local neural activity results in a locally increased energy requirement, that increases the metabolic rate of oxygen consumption. This leads to an increase in the cerebral blood flow and vasodilation to restore the local oxygen levels. Oxygen is transported in the bloodstream by haemoglobin within red blood cells. Depending on its oxygenation state, haemoglobin exists in two forms: oxyhaemoglobin, which is bound to 4 oxygen molecules, and deoxyhaemoglobin, in which the binding sites for oxygen are vacant. Both oxyhaemoglobin

and deoxyhaemoglobin contain an iron atom, but the absence of oxygen in deoxyhaemoglobin leads to a different electronic configuration of the iron, characterized by unpaired electrons. This results in different magnetic properties. Deoxyhaemoglobin is paramagnetic, leading to field inhomogeneities in the magnetic field surrounding the red blood cells. These field inhomogeneities are responsible for the acceleration in the decay of transverse magnetization and shortening of the T2* relaxation, therefore reduction to image intensity (Chen et al., 2023; Glover, 2011).. Oxyhaemoglobin, instead, is diamagnetic and does not disturb the magnetic field. The variation in relative concentration of these two forms reflect the changes in oxygen delivery and consumption in active brain regions. Therefore, the BOLD signal relies on sensitivity to changes in oxygen levels within the circulating blood (Casey et al., 2002).The temporal evolution of the hemodynamic response is commonly modelled in fMRI analyses by the Hemodynamic Response Function (HRF – Figure 7), a mathematical model that represents the characteristic shape of the BOLD signal over time (G. Chen et al., 2023a). Following a neural event, there is an initial increase of deoxyhaemoglobin (dHb) and a decrease in oxyhaemoglobin (HbO2), due to the initial consumption of the oxygen in response to the event (Figure 7 - initial dip). Within one or two seconds, the situation is reversed by a vasodilatory response that increases the cerebral blood flow (rise of the signal in Figure 7), leading to an increase in HbO2, that exceeds the oxygen demand, and decrease in dHb. This sequence of events describes the hemodynamic response to a stimulus (Glover, 2011).

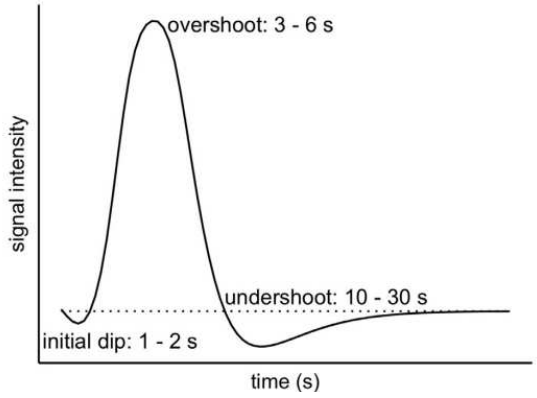

Figure 7. Typical Bold response modelled as a Hemodynamic Response Function (HRF): after the stimulus onset, there is an initial dip in the signal, that can last up to one second and is an indication of oxygen consumption. Followed by a rise in the signal, the 'overshoot', that reaches its peak after approximately 4-6s. Finally, the signal falls under the baseline and then returns to the baseline (G. Chen et al., 2023b).

2.2 Overview of Task-based fMRI

There are two main modes of fMRI acquisition, resting-state fMRI (rsfMRI) and task-based fMRI. In rsfMRI, the subject is scanned in the absence of any sensory or cognitive stimulus (e.g., without performing any specific task), allowing the assessment of spontaneous brain activity (Smitha et al., 2017). In task-based fMRI, the subject performs a specific cognitive or motor task during scanning, to evoke localized brain activations, thus enabling the investigation of brain responses associated with the experimental condition. The use of fMRI with task-based or stimuli-driven paradigms is crucial for the brain function studies, allowing the identification of brain regions activated by changes in the baseline of the BOLD signal during task performance or response to stimuli (Wei et al., 2024). In common fMRI task-based protocols, participants are required to perform a cognitive, sensory or motor task while MRI volumes are collected. The experimental paradigm is thus designed to manipulate neural activity in a controlled manner, as the aim is to induce two or more cognitive states, to test the hypothesis that the BOLD signal differs between these states. In the simple case with two states, one state is denoted as the experimental condition while the other is the control condition. The two experimental designs mainly used in fMRI are block design and event related design, which are schematically illustrated in Figure 8.

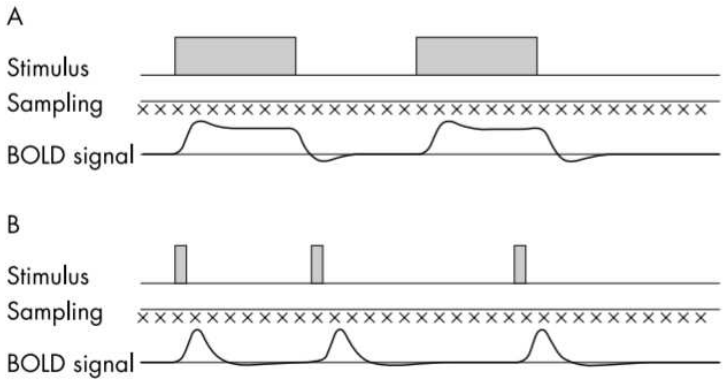

Figure 8. Schematic representation of a block design functional magnetic resonance imaging (fMRI) paradigm (A) and an event related fMRI paradigm (B). For the block design the stimulation period (e.g., 30s) is alternated with a control period. For the event related design, a brief stimulus period is used, which can either be periodic or randomised. In both cases volumes of data (indicated by the crosses) are collected continuously (Matthews & Jezzard P, 2004).

In a simple block design, condition and controlled/resting states are alternated, with each block being a few seconds long ($\geq 10s$). The advantage is this design is that the activity-related signal change observed in block design fMRI is generally quite high. However, several drawbacks relate to the sustained stimulus during the condition blocks as it may introduce confounding factors such as habituation or expectation and discards temporal information about individual hemodynamic response functions to specific stimuli. Moreover, in clinical settings, for a patient could be difficult to perform a block-design task. In the event related design task events are relatively short ad occur at different Inter Stimulus Intervals (ISI), which can go from 2 to 10 seconds. The time jittering allows to sample the hemodynamic response with a higher frequency in the overall time series and is an efficient strategy for example toprevent anticipatory response and maintain attention. An event related design is thus more suitable for the characterization of the timing and the amplitude of the hemodynamic response since stimuli are presented individually and the corresponding hemodynamic responses are measured separately (Glover, 2011; Sexton et al., 2013).

2.3 fMRI Data Acquisition

Functional MRI studies are mostly performed on scanners at 3T for both clinical and research purpose, which provide and optimal balance between signal to noise ratio (SNR) and resolution, although higher field strengths are increasingly used for research. Since the goal is to detect rapid changes and increase the sensitivity to T2* changes, most fMRI data is obtained using T2* Gradient Echo - Echo Planar Imaging (GE-EPI) sequences. This technique allows the collection of the two-dimensional image by changing spatial gradients rapidly following the excitation pulse. Acquisition parameters used in these sequences, influence the quality of the data and the sensitivity to the desired signal. The TR defines the temporal resolution of the experiment, corresponding to the time between two consecutive acquired volumes. Typical TRs for whole brain scans range from 2000-3000ms. The TE is usually chosen to approximate the T2* of gray matter (25-35ms) to maximize the BOLD contrast. The voxel size is usually between 2.5 and $3.5mm^3$. The field of view (FOV) (i.e., the spatial extent of the acquired slice), is usually $\sim 220 \times 220\ mm^2$, with 30-40 slices acquires. In task-based fMRI each acquisition typically lasts 3-6 min (Koc et al., 2026).

During fMRI acquisition, each volume is acquired slice by slice. There are different acquisition schemes, ascending, descending and interleaved. In the ascending acquisition scheme slices are acquired in sequential order from the bottom (i.e., neck) to the top of the head, and inverse order in the descending acquisition scheme. In the interleaved acquisition scheme slices are acquired in alternating order (e.g., first odd slices, then even slices). This last approach reduces crosstalk between adjacent slices, as slice selection might affect neighbouring spins. Since slices are not acquired simultaneously, this is accounted for in the preprocessing procedure, particularly in the slice timing correction described in the next chapter (2.4 Preprocessing of fMRI Data).

In studies involving fMRI acquisitions, anatomical scans as the T1-weighted images are also acquired, providing detailed anatomical information that can be used both for preprocessing steps and to associate a recorded activation to a precise region with higher anatomical accuracy.

2.4 Preprocessing of fMRI Data

Once raw fMRI data is acquired, the time series must be pre-processed to prepare the data for the statistical analysis and to obtain maps of brain activation related to the task. The BOLD signal is affected by thermal or system noise depending on the acquisition set-up, as well as systematic and physiological noise (e.g., head movement and cardiac movement respectively). The goal of the preprocessing is to remove the systematic and non-task related sources of variability while preserving the BOLD signal (Glover, 2011; Gregory Ashby, 2015).The conventional steps in preprocessing include the following:

(1) Slice-time correction, which temporally aligns the slices within each acquired volume to reference time point (e.g., the acquisition time of the first slice). This step is particularly important to capture temporal dynamics of the BOLD response in task-based fMRI.
(2) Realignment, also referred to as Motion Correction, where rigid body transformations are estimated and applied to align all the fMRI volumes to a reference, this correction accounts for head movements.
(3) Coregistration, which aligns subject specific structural and functional data.
(4) Normalization, which consists of registering anatomical and functional data to a common space. This allows comparisons at group level between subjects, as there are intersubject

differences (e.g., brain size and shape) which do not allow direct comparison in the original acquisition space, called the native space. The most used reference system is the Montreal Neurological Institute (MNI) space, derived from averaging anatomical brain acquisitions from many subjects. This step is also important for the definition of VOIs. Normalization is achieved through affine and nonlinear transformations. Affine transformation includes translations, rotations, scaling and shearing, and accounts for global differences between native image and MNI templates. Nonlinear transformations account for local anatomical differences, allowing to define voxel wise deformations.

(5) Nuisance regression refers to the modelling and removal of unwanted variance in the signal (i.e., correction for physiologic noise from breathing and cardiovascular function).

(4) Spatial smoothing to improve the signal to noise ratio (SNR) and improve the normality of the noise distribution.

(6) Low pass and/or high pass temporal filtering to improve the statis-tics while removing spectral components of no interest, while maintaining characteristic frequencies of the Bold signal.

Among preprocessing steps, temporal filtering plays an important role as it can affect the spectral content of the BOLD signal. The specific preprocessing pipelines applied for the case study is described in Material and Methods (5.4 fMRI Data Preprocessing).

2.4.1 Spectral content of the BOLD signal

It is well established in literature that physiologically meaningful oscillations in the BOLD signal, are predominantly below 0.1 Hz, these frequencies are referred to as low frequency oscillations (LFOs). Particularly, researchers have consistently identified coherent spontaneous LFOs in the 0.01–0.1 Hz range, during both resting and active-task conditions (Cordes et al., 2001; Zuo et al., 2010). Thus, fMRI data are commonly bandpass (e.g., 0.01–0.08 Hz) filtered (e.g., 0.01–0.08 Hz) to reduce the effect of very low frequency and high frequency physiological noise (Chao-Gan & Yu-Feng, 2010). Physiological processes such as respiration occur at higher frequency ranges relative to the LFOs (∼0.1-05 Hz and ∼0.6-12 Hz respectively), but can artifactually appear even at low frequencies due to aliasing. However, as highlighted by Cordes et al., 2001, low-pass filtering may suppress not only physiological noise but also meaningful information, as neural related information may also be present at frequencies above 0.1 Hz.

Moreover, researchers proposed a subdivision in difference frequency bands, as oscillations within specific ranges have been linked to a variety of neural processes, such as emotional regulation, attention and memory. Therefore, typical BOLD fluctuations were thoroughlyhave been subdivided into frequency bands such as Slow-5 (0.01-0.027 Hz), Slow-4 (0.027-0.073 Hz) and Slow-3 (0.073-0.198 Hz), which have been associated with distinct neurophysiological processes. Slow-5 and Slow-4 (0.01–0.073 Hz) were primarily detected within gray matter, while relatively higher frequencies of Slow-3 were detected within white matter. Slow-5 oscillations are generally associated with larger scale dynamics, while Slow-4 is considered to reflect intrinsic neural activity and between regions synchronization (Zuo et al., 2010). Slow-3 band is in a higher frequency range and is therefore more susceptible to physiological noise, however, although with reduced amplitude, BOLD fluctuations may extend to these higher frequencies (J. E. Chen & Glover, 2015).

2.5 Statistical Analysis and General Linear Model

After the preprocessing, data can undergo statistical analysis to identify brain regions activated by the specific task considered in the experimental paradigm. Statistical data analysis is often carried in two steps, a first-level analysis of data from each subject, followed by a second-level analysis in which results from multiple subjects, that undergo the same fMRI experiment, are combined (Gregory Ashby, 2015; Monti, 2011). The General Linear Model (GLM) is one of the most used approaches for fMRI data analysis. In the context of task-based fMRI, the GLM is used to perform statistical inferences by applying univariate tests for each voxel, to assess whether an experimental condition is significantly reflected by the measured BOLD signal in that voxel. In practice each voxel is analysed by a parametric statistical test (t-test or F-test), then the resulting statistics are assembled into spatial maps known as Statistical Parametric Maps (SPMs), which denote brain regions that show significant activations (K. Friston et al., 1995). Given that the measured signal from each voxel is a combination of different contributions due to experimental conditions, as well as noise and other sources of variability, the goal of the GLM is to model these components separately.

2.5.1 Theoretical framework of the General Linear Model

In this approach, the BOLD signal associated with each voxel is modelled as a weighted sum of known predictor variables, which are factors that are hypothesized to contribute to the activation of a voxel (i.e., the time series extracted), plus an error term. The aim of the analysis is to estimate the contribution of each predictor, also called regressors, to the variability observed in the time series extracted from each voxel. If there a *n*-volumes acquired, the BOLD response y, is sampled *n*-times. Thus, the intensity of the BOLD signal y_i at the i-th observation time can be represented by the linear combination of p regressors:

$$y_i = x_{i,1}\beta_1 + x_{i,2}\beta_2 \dots x_{i,p}\beta_p + \varepsilon_i \tag{11}$$

where $x_{i,1} \dots x_{i,p}$ are the regressors weighted by the weight parameters $\beta_1 \dots \beta_p$ which indicate how much each regressor contributes to the signal y_i. The residual noise in the data,

or error in the measurements, is ε_i. In fMRI, the model is applied voxel-wise where the measured BOLD time series is modelled in a matrix form as:

$$Y = X\beta + \varepsilon \tag{12}$$

Where Y is an $n \times 1$ column vector, that contains the time series across the n time points for one voxel (n = number of volumes acquired) , X is the $n \times p$ design matrix, β is the $p \times 1$ vector of unknown weight parameters to estimate, ε is an $n \times 1$ vector containing the error values associated with each observation. The predicted data is thus described. It is important to note that the design matrix encodes the experimental design, where regressors of interest relative to the task are constructed by a convolution of the stimuli paradigm and the HRF.

The design matrix also includes additional regressors, called nuisance regressors, that account for head motion, slow temporal drifts and baseline signal intensity in the time series (Monti, 2011). A schematic depiction of the GLM is shown in Figure 9

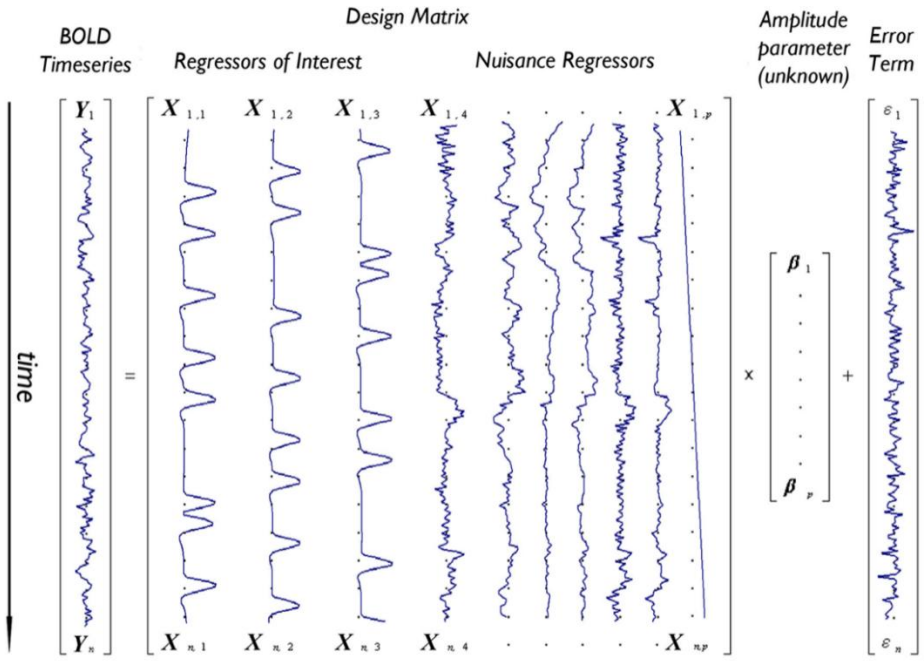

Figure 9. Depiction of the GLM model for an imaginary voxel with time-series Y predicted by a design matrix X including 10 effects (three regressors of interest e.g., three tasks, and seven nuisance regressors e.g., six motion parameters and one linear drift) of unknown amplitude β_i and an error term (Monti, 2011).

One of the simplest methods to estimate the unknown β parameters is the Ordinary Least Squares (OLS) method. The goal of the method is to minimize the sum of the squared

residuals or errors, defined as the squared difference between the measured signal Y and the expected signal given by the X matrix scaled by β: $min \sum_{i=1}^{n} (Y_i - X_i \times \beta)^2$. The solution of this minimization is given by the following estimation for the unknown parameters and their variance:

$$\hat{\beta} = (X^T X)^{-1} X^T Y \tag{13}$$
$$var(\hat{\beta}) = \sigma^2 (X^T X)^{-1}$$

Where $\hat{\beta}$ are the estimated parameters and σ^2 is the variance of the residual errors. These expressions are derived under the assumption that errors are independent and identically distributed (i.i.d) according to the normal distribution $\sim N(0, \sigma^2 I)$. In other words, the model assumes that each scan is statistically independent, which is often untrue for fMRI data. Other assumptions regard the regressors in the X matrix, stating that they must be known, deterministic and independent of error, and that no regressor is a linear transformation of other regressors.

Following parameter estimation, statistical inference can be performed to test hypotheses about experimental effects. These hypotheses are defined by contrasts, which allow to isolate specific effects of interest and are represented by a linear combination of the estimated β parameters or regressor coefficients:

$$c^T \beta \tag{14}$$

Where c is the contrast vector $p \times 1$. The significance of a specific effect can be done by using the t-statistic which follows a t distribution and is defined as:

$$t = \frac{c^T \beta}{\sqrt{\hat{\sigma}^2 \, c^T \, (X^T X)^{-1} c}} \tag{15}$$

Null hypothesis $H_0: c^T \beta = 0$ states that the effect of interest does not significantly explain any variance in the model. The alternative hypothesis is $H_1: c^T \beta \neq 0$.

When multiple parameters are tested simultaneously, statistical inference can be performed using F-statistics, which evaluates if a set of q regressors that jointly explain a significant portion of the variance in the observed signal. In this case the contrast is matrix C $[p \times q]$, and the F - distribution is expressed as:

$$F = (C^T\hat{\beta})[C^T(X^TX)C]^{-1}(C^T\hat{\beta})/q\hat{\sigma}^2 \quad (16)$$

Here the null hypothesis states that multiple parameters do not jointly explain any variance in the data.

Statistical analysis is applied voxel wise. Resulting t-values or F-values from all voxels constitute a SPM, which represent a spatially extended statistical process that directly reflect the significance of the regressors. This allows to identify and visualize regions with statistically significant activations in task-related fMRI experiments (K. Friston et al., 1995).

Once single-subject data has been analysed, individual results are aggregated to assess commonalities and stability of effects within or across groups of subjects with the second-level analysis (Monti, 2011). Given the wide variability in shape and size of the adult human brain, normalization is a crucial preprocessing step before proceeding with this analysis. Second level analysis does not use the timeseries, but the contrast maps obtained from the first level analysis. These contrast maps summarize the effect of a task or condition for each subject. Considering an experiment with N subjects, for each voxel v, the considered data is $Y_v = [c_1\ c_2 \dots c_N]^T$, where c_k is the contrast value at voxel v for the k-th subject. The GLM model at the group level can be expressed for each voxel as:

$$Y_v = X\beta_v + \varepsilon_v \quad (17)$$

Where X is the design matrix of size $N \times$ p, with p being the number of groups, β_v parameters usually representing the mean effects, ε_v are the residuals.

3. Dynamic Causal Modelling

Dynamic Causal Modelling (DCM) is one of the most used methods for inferring effective connectivity from neuroimaging data, such as task-based functional magnetic resonance imaging (fMRI). Effective connectivity refers to the directed causal influences that one brain region exerts over another (Stephan et al., 2010). There are other connectivity characterizations that can be distinguished, such as structural connectivity and functional connectivity. Structural connectivity concerns the physical architecture of brain regions in terms of synaptic connections and white matter tracts. Functional connectivity describes statistical dependencies between brain regions (e.g, correlation), without implying any casual relationships. Effective connectivity is not typically observed directly, therefore DCM links hidden neural activity at a microscopic level to macroscopic measurements, such as the BOLD signal acquired with fMRI.

DCM provides a generative modelling framework, used to specify and compare hypotheses about effective connectivity by estimating model parameters that explain the observed data through Bayesian inference. Particularly, the aim is to estimate and make inferences about the strength and direction of connections between brain regions and how this coupling is modulated by experimental manipulations. It is important to note that since, DCM is used to test specific hypotheses driven by the experimental design, the effective connectivity estimated is specific to the stimuli employed in the experiment. The model therefore is the formalisation of the hypothesis on what generated the data (K. J. Friston et al., 2003; Zeidman et al., 2019). These aspects will be thoroughly discussed in the following sections.

3.1 Theoretical Framework of Dynamic Causal Modelling

The main idea behind the dynamic causal modelling is to treat the brain as deterministic nonlinear dynamical system, which is subjected to inputs and produces measurable outputs. The forward generative model typically used with task-based fMRI experiments is shown in Figure 10, and represents the hypothesis of the underlying neural activity that better explains the acquired data given certain experimental stimuli.

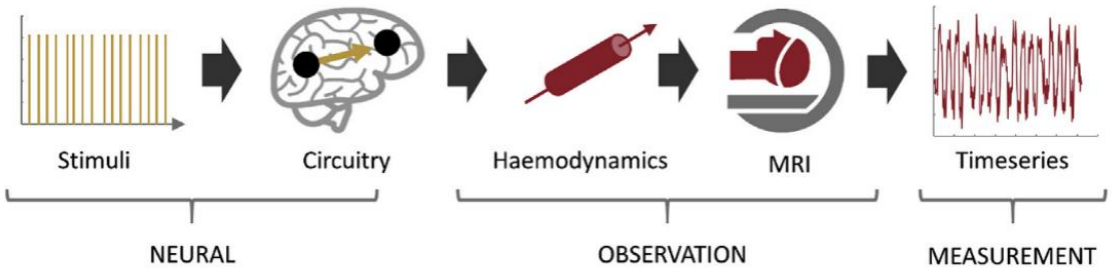

Figure 10. The forward (generative) model in DCM for fMRI. The model is split into three parts: neural, observation (haemodynamic, BOLD signal components) and measurement (the addition of observation noise). The neural model is driven by experimental stimuli, specified as short events (delta functions). The resulting neural activity causes a change in blood flow, mediated by neurovascular coupling, and consequently the generation of the BOLD signal. The addition of observation noise gives the fMRI timeseries (Zeidman et al., 2019).

Experimental conditions are encoded by stimuli in a typical task-based fMRI experiment (e.g., stick or boxcar functions as for onset time in the design matrix in GLM) and represent the known inputs that elicit the hypothesized region-specific activations and interactions among regions. The regions involved are called regions of interest (ROIs), or volumes of interest (VOIs), which can be seen as nodes in a schematic representation of the brain as a network of interconnected regions. In this representation, the edges are the values of the effective connectivity matrix estimated in DCM framework as detailed below. The experimental stimuli drive a neural model, which predicts the resulting change in neural activity over time. The neural model is tuned by a vector of parameters $\theta^{(n)}$, where superscript (n) denotes that these are *neural* model parameters, which describe the strength of connections, i.e., the values of the effective connectivity. DCM model inversion estimates the values of $\theta^{(n)}$, by simulating neuronal activity using a neuronal model (details in section 3.1.1) and convolving it with a HRF (i.e., haemodynamic model), to obtain a simulated BOLD signal. Parameters $\theta^{(n)}$ are iteratively changed and model inversion applied for each $\theta^{(n)}$ configuration until the simulated BOLD signal matched the experimental recordings with a pre-defined tolerance.

Following the framework described by Zeidman et al. (2019), the generative model of DCM can be expressed as neural model (18) and a haemodynamic model (19) describing the transformation of neural activity into the BOLD response:

$$\dot{z} = f\left(z, u, \theta^{(n)}\right) \tag{18}$$

$$y = g\left(z, \theta^{(h)}\right) + X_0\beta_0 + \varepsilon \tag{19}$$

In equation (18), f is the neural model that describes neural dynamics, which specifies how the change in neural activity over time $\dot{z}$ is caused by experimental stimuli u, current neural state z, and neural connectivity parameters $\theta^{(n)}$. Vector z encodes the neural activity within the considered brain regions; thus, it represents the hidden states that cannot be directly observed in the fMRI data. In equation (19), y is the measured BOLD signal and is modelled as the sum of different contributions: function g is haemodynamic model, which describes the neurovascular coupling transforming neural activity z into the BOLD response through the parameters $\theta^{(h)}$ where superscript (h) denotes that these are *haemodynamic* parameters; the design matrix X_0 and β_0 parameters, which capture uninteresting effects such as the mean of the signal; the observation noise ε, which captures the variability in the measured BOLD which the model does not explain.

3.1.1 Neural model

In DCM for fMRI, the neural model in equation (20), is a Taylor approximation of function f, described as the following bilinear state equation:

$$\dot{z} \approx \left(A + \sum_k B^{(k)} u_k(t)\right) z + Cu(t) \tag{20}$$

Where the different contributions that determine the temporal evolution of neural activity $\dot{z}$, are separated. Parameter matrix A specifies the baseline or intrinsic effective connectivity; it is also referred to as the fixed connectivity matrix. These parameters describe the overall influence of one region on another and it does not depend on the duration of the stimulus. Matrices $B^{(k)}$ specify the modulation of effective connectivity due to the modulatory inputs $u_k(t)$, where index k denotes the different modulatory inputs included in the model. Matrix C represents the influence of driving inputs $u(t)$ on the neural activity. The set of parameters $\theta^{(n)} = \{A, B^{(k)}, C\}$ is measured in Hz and defines the effective connectivity of the network. The structure of these matrixes needs to be specified, in terms of which region is hypothesised

to be connected to which, and subsequently the strength of connections is estimated from the observed data during model inversion.

3.1.2 Hemodynamic model

In fMRI experiments the BOLD signal is not a direct measure of neuronal activity but rather reflects this activity through the neurovascular coupling, which links neuronal activity to the hemodynamic response. The model adopted in DCM to describe the neurovascular coupling is the Balloon-Windkessel model, proposed by Buxton et al., (1998). This model is here discussed considering the formulation offered by Friston et al., 2003:

$$\begin{aligned} \dot{s}_i &= z_i - k_i s_i - \gamma_i (f_i - 1) \\ \dot{f}_i &= s_i \\ \tau_i \dot{v}_i &= f_i - v_i^{1/\alpha} \\ \tau_i \dot{q}_i &= f_i E(f_i, \rho_i)/\rho_i - v_i^{1/\alpha} q_i / v_i \end{aligned} \tag{21}$$

In the formulation (*21*), neuronal activities in each brain region drive a set of haemodynamic state variables. In the first equation, neuronal activity z_i of the i-th region, induces a vasodilatory signal s_i, which has a rate of decay k_i and is subjected to an autoregulatory feedback with strength γ_i, linked to blood inflow f_i. Second expression states that the vasodilatory signal s_i drives the changes in blood inflow f_i. Third equation states that the variations in blood volume $\dot{v}_i$, depend on the difference between inflow f_i and outflow $v_i^{1/\alpha}$ where α is Grubb's exponent. Parameter τ_i is the mean transit time of blood through the venous compartment. The fourth equation describes the variation of deoxyhaemoglobin level q_i. In particular that $\dot{q}_i$ depends on blood inflow f_i, oxygen extraction function $E(f, p) = 1 - (1 - p)^{1/f}$, where ρ_i is resting oxygen extraction fraction, and oxygen removal with trough blood outflow, which depends $v_i^{1/\alpha}$ and q_i/v_i.

The BOLD signal can be modelled as a nonlinear function (*22*), which depends directly on the blood volume v_i and deoxyhaemoglobin content q_i, while the other variables (s_i, f_i) link neuronal activity to the hemodynamic response.

$$y_i = g(q_i, v_i) = V_0[k_1(1 - q_i) + k_2\left(1 - \frac{q_i}{v_i}\right) + k_3(1 - v_i)] \tag{22}$$

$$k_1 = 7\rho_i$$
$$k_2 = 2$$
$$k_3 = 2\rho_i - 0.2$$

In expression (*22*), $V_0 = 0.02$ is resting blood volume fraction. The hemodynamic parameter vector $\theta^{(h)} = \{k, \gamma, \tau, \alpha, \rho\}$ contains the biophysical parameters previously described. A schematic representation of the haemodynamic model is shown in Figure 11.

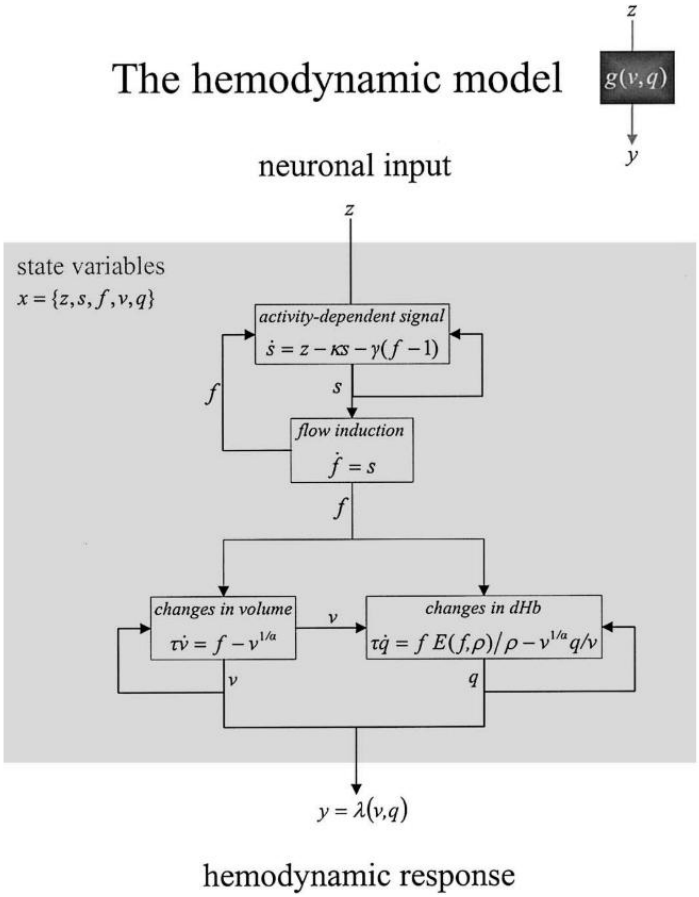

Figure 11. Schematic representation of the haemodynamic model used by DCM for fMRI. Neuronal activity induces a vasodilatory and activity-dependent signal s that increases blood flow f. Blood flow causes changes in volume and deoxyhaemoglobin (v and q). These two haemodynamic states enter the output nonlinearity which results in a predicted BOLD response y. The model has 5 hemodynamic parameters: the rate constant of the vasodilatory signal decay (κ), the rate constant for auto-regulatory feedback by blood flow (γ), transit time (τ), Grubb's vessel stiffness exponent (α), and capillary resting net oxygen extraction (ρ). E is the oxygen extraction function (K. J. Friston et al., 2003).

3.2 Model specification and estimation

As for now it is clear that DCM defines the generative model that describes how hidden neural states interact and how they give rise to the observed BOLD signal. This requires the definition of the structure of the brain network and the experimental inputs which drive the system. When specifying the model, one needs to define the VOIs included in the network, which are the nodes of the network, and define the architecture of the intrinsic connections between them. Definition of this structure can be informed by previous knowledge upon regions that might be involved, this allows to reduce model complexity and allows for meaningful inference (Stephan et al., 2010). The ensemble of matrices A, B and C defines the hypothesized causal architecture of the network to be tested. DCM is a hypothesis-driven framework, meaning that multiple models can be specified to test alternative hypotheses regarding the causal connections (i.e., effective connectivity) which determine the observed data.

Once the generative model is specified the next step is model inversion for each subject. In this process the parameters $\theta^{(n)}$ are estimated relying on finding the best trade-off between model accuracy and model complexity. Model accuracy describes how well the predicted timeseries fit to the measured data. Model complexity describes how much the parameters change from the prior value in order to describe the measured data. DCM uses Bayesian inference to estimate the parameters, in which prior beliefs on the parameters are combined with the observed data to obtain their posterior probability. Priors and posteriors on $\theta^{(n)}$ and $\theta^{(h)}$ are represented by probability densities. Typically, these are Gaussian distributions characterized by their mean and variance, which reflect the expected value and the respective uncertainty. Neural connectivity priors are used mainly to ensure the stability of the model by introducing a constraint on these values. Thus, priors on $\theta^{(n)}$ have a zero mean and relatively small variance, this reflects the assumptions that if there is not strong evidence from the data the connections are weak(K. J. Friston et al., 2003; Zeidman et al., 2019).

The trade-off between accuracy and complexity is obtained by maximizing the log model evidence $\log \mathrm{p}(y|m)$, which is the logarithm of the model evidence $\mathrm{p}(y|m)$. The model evidence expresses the probability of obtaining the observed data y given a particular model

m. In general, the computation of the model evidence requires the integration over all possible parameters θ:

$$p(y|m) = \int p\ (y|\theta, m)\ p(m|\theta) d\theta \tag{23}$$

The model evidence is analytically intractable and numerically difficult to compute; therefore, it is usually calculated through an approximation, called Free Energy (F). F can be conceptually described as the difference between an accuracy term and a complexity term. By minimizing F through an iterative optimization procedure, parameters are estimated until convergence. When convergence is reached, the procedure gives in output the posteriors on model parameters and approximation of the model evidence. Model evidence obtained from model inversion is used for subsequent evaluations where models are compared.

3.3 Bayesian Model Selection

For any experimental observation, there are infinite models that could explain the data. The purpose of model selection is to find which model, of the set of possible alternatives, better represents a balance between accuracy and complexity, thus affording maximal generalizability. This is done through Bayesian Model Selection (BMS), which is based on the previously explained model evidence $\mathrm{p}(y|m)$ approximated by F during model inversion. Given one subject and two models m_1 and m_2, BMS can be done through the Bayes Factor (BF), defined as the ratio of their model evidence. Considering the logarithm of BF, it can be approximated to the difference between F of the two models:

$$\log BF_{i,j} = log \frac{p(\mathrm{y}|\mathrm{m_i})}{p(y|m_j)} \approx \Delta F_{i,j} = F_i - F_j \tag{24}$$

Where a positive value indicates evidence in favour of model m_i that best explains the acquired data y, and a negative value is in favour of model m_j. The magnitude of the difference is the strength of the evidence in favour of one model (Stephan et al., 2010).

In group studies, where multiple subjects are considered BMS can be implemented with two different approaches, fixed effects (FFX) and random effects (RFX), under different assumptions. In the FFX approach, the assumption is that all N subjects share the same model structure, an assumption warranted when studying basic physiological mechanisms that are unlikely to vary across subjects. Under FFX assumption, the metric used to perform the BMS

is the Group Bayes Factor (GBF), obtained as the product of the individual Bayes Factors across subjects:

$$GBF_{i,j} = \prod_{n=1}^{N} BF_{i,j}^{(n)} \tag{25}$$

Where i,j refer to the models compared for the n-th subject (Stephan et al., 2009, 2010)

RFX accounts for heterogeneity in the model structure across subjects. This assumption is more appropriate, as an example, when dealing with cognitive task that can be performed with different cognitive strategies across subjects. Within RFX assumptions, it is possible to estimate the Exceedance Probability (EP), which quantifies the probability that one model is more likely in the population of any other model tested:

$$EP_i = p\left(r_i > r_j \ \forall\, j \neq i \middle| y\right) \tag{26}$$

Where r_i denotes the frequency of model m_i in the model population. A more conservative metric is the Protected Exceedance Probability (PEP), that accounts for the possibility that differences in the models may arise by chance. To establish a representative group model, in the case where BMS indicates an optimal model for the subjects, Bayesian model averaging (BMA) is used to compute the average parameter estimates across the optimal models for the subjects (Stephan et al., 2010).

4. Aim of the Thesis

As described in the Introduction Chapters, task-based fMRI experiments rely on the analysis of the BOLD signal to investigate temporal dynamics of underlying neuronal activity. Accurate extraction of this signal is important for reliable neuroimaging analyses; therefore, fMRI data undergo a series of preprocessing steps to reduce noise and isolate relevant signal components. Among these steps, temporal filtering is commonly used within fMRI, especially rsfMRI, preprocessing pipeline to retain relevant BOLD frequency components (<0.1 Hz), while attenuating physiological noise. In task-based fMRI filtering usage is less consistent. Particularly, previous studies which investigated the visuomotor network with task-based fMRI have employed different preprocessing strategies. For example, for the same acquired data Lorenzi et. al 2025 used a bandpass filter in the preprocessing pipeline while the preprocessing pipeline in Alahmadi et. al 2016 did not include the temporal filtering. These methodological difference raises the question whether and to what extent the temporal filtering impacts BOLD signal properties and subsequent analyses as within the DCM framework.

Therefore, the aim of this thesis is to assess the impact of the temporal bandpass filter on both the BOLD signal and the estimation of the fixed effective connectivity using DCM, focusing on regions involved in the visuomotor task. The analysis was conducted on the same fMRI data in visuomotor task employed in the two previously mentioned studies. Specifically, this study aims to evaluate different filtering strategies involving the use of a bandpass filter (0.008 – 0.09 Hz), by analysing unfiltered, bandpass filtered before VOI extraction, and after VOI extraction. The behaviour and effectiveness of the bandpass are first characterized on synthetic signal, with power spectral density analysis.

5. Materials and Methods

5.1 Participants

The analysis was performed on twenty-one right-handed healthy volunteers with no history of neurological or psychiatric disorders, who had already been included in previous investigations(Alahmadi et al., 2016; Casiraghi et al., 2019; Lorenzi et al., 2025). The twenty-one participants (mean age: 22 ± 4 years, 9 males) were enrolled in a visuomotor execution task (i.e., AE – Action Execution paradigm). All participants gave their written informed consent and received a detailed explanation of the experimental procedure before participating.

5.2 MRI Acquisition Protocol

In this study, acquisitions were made using a 3 T Philips Achieva system scanner (Philips Healthcare, Best, The Netherland) with a 32-channel head coil. The imaging protocol included for each subject a 3D T1-weighted anatomical scan and three BOLD sensitive T2*-weighted GE-EPI fMRI series, characterized as following:

1. T1-weighted volume (3D-T1): 3D inversion-recovery gradient-echo (fast field echo) with inversion time (TI) = 824 ms. TE = 3.1ms, TR = 6.9ms, flip angle = 8°, voxel size = $1 \times 1 \times 1\ mm^3$.
2. T2* - weighted GE-EPI fMRI series: TR = 2500 ms, TE = 35 ms, flip angle = 90°, voxel size = $3 \times 3 \times 3\ mm^3$, number of slices = 46 acquired with descending order, number of volumes = 200, FOV = $192 \times 192\ mm^2$.

5.3 fMRI Paradigm

The experimental design described in (Alahmadi et al., 2016) consisted of a visually guided event-related power grip task, where participants used their right (dominant) hand to squeeze a rubber ball with varying grip force (GF) levels (Figure 12). The rubber ball used to perform the task (Figure 12.a), was a MR-compatible sphygmomanometer inflation bulb connected to a computer suite outside the scanner room. The ball compression resulted in air pressure measurement proportional to the exerted force, recorded at a 20Hz sampling rate. The force measurement system consisted of an USB-1608FS data acquisition device connected to the pressure transducer (0-$1.0342 \times 10^5\ Pa$. Each experiment consisted of 75 active trials,

equally divided into 15 sets of different GF levels, corresponding to 20%, 30%, 40%, 50% and 60% of the maximum voluntary contraction (MVC). For each subject MVC has been recorded prior to the experiment with the same force measurement system and used to set the GF target. The GF trials, which lasted 3 s each, were interleaved by rest intervals, which lasted between 2 – 12 s randomly and comprised 55% of the fMRI session (500s). The order of GF trials and rest periods were optimized, to introduce temporal jittering and GF presented in counter-balanced and randomised order.

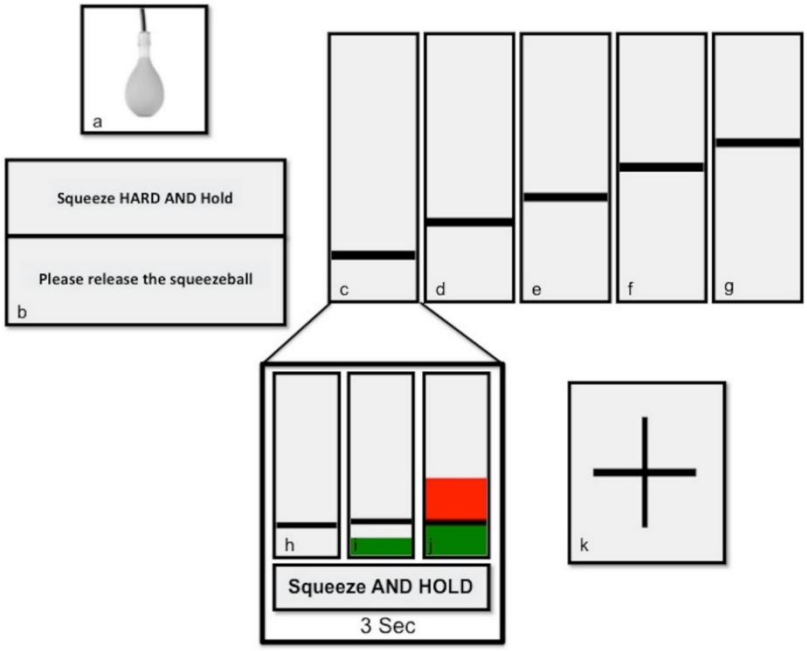

Figure 12. The diagram describing the steps that each subject followed. (a) The rubber flexible compatible MRI squeezeball;(b) instructions for measuring each subject's MVC prior to scanning; (c–g) the anonymous GF levels starting from 20 % with a step of 10–60 % of MVC.(h–j) Examples of a cued trial where (h) is the cue starting with an instructed sentence "Squeeze AND HOLD", (i) is an example indicating that the response has not reached the required GF level while (j) shows that the response exceeds the required GF level and a red bar warns subjects. Lastly, (k) shows a cross sign indicating a rest time (Alahmadi et al., 2016).

The visual cue shown during the experiments was a black static horizontal bar indicating the target GF to reach, together with a coloured bar indicating the actual GF reached, thus providing visual feedback (i.e., green colour if GF exerted is $\leq$ target GF, red otherwise, Figure 12.h-j). Rest intervals were cued by a crosshair (Figure 12.k) at the centre of the screen. Subjects were asked to match the height of the horizontal line by controlling their GF and once target was reached to hold it until the crosshair appeared. The visual cues projected during the experiment on a MR compatible screen inside the scanner room and viewed by the participant through a mirror placed on the head coil. Before the fMRI session, subjects were trained using a similar but different design (2 min) with GF levels ranging between 10-70% of their MVC. In the training session, participants firstly observed the task being performed.

5.4 fMRI Data Preprocessing

The preprocessing of the fMRI images was done with MATLAB, using different neuroimaging tool: SPM12 (https://www.fil.ion.ucl.ac.uk/spm/), FSL (https://fsl.fmrib.ox.ac.uk/fsl/fslwiki) and MRtrix3 (https://www.mrtrix.org/). The complete preprocessing pipeline implemented for this study follows the approach adopted by Lorenzi et al., 2025 for this dataset, ensuring consistency in the methodologic approach. In addition to the standard pipeline illustrated in Chapter 2.4, this pipeline includes an initial step of thermal noise removal and are applied as follows:

(1) Thermal noise removal: thermal noise was removed from raw fMRI acquisitions using Marchenko Pastur - Principal Component Analysis (MP-PCA), used to separate random noise across voxels from the true signal. This method applies PCA to groups of neighbouring voxels and analyses the distribution of resulting eigenvalues. Eigenvalues that follow MP distribution are assumed to characterize pure noise. This algorithm is applied with the of the *dwidenoise* tool of MRtrix3. A noise map is thus obtained aside with denoised fMRI data.

(2) Slice-timing correction: this second step was applied to the denoised fMRI data. Firstly, the 4D fMRI data were split into separate 3D volumes using FSL (*fslplit*). Then SPM's *spm_slice_timing* function is applied to the volume, obtaining in output the time corrected volumes, in which each slice results to be aligned with the acquisition time of the first slice. The corrected volumes are then recombined into a single 4D file using FSL (*fslmerge*).

(3) Realignment: is applied to the time corrected volumes. Here the SPM's *spm_realign* function was used to estimate 6 rigid body transformation parameters to align all functional volumes to the common reference (i.e., the first volume).The SPM function generates in output the spatially corrected volumes, the mean fMRI of the corrected volumes and the 6 estimated motion parameters, which will be used in the next steps of the pipeline.

(4) Coregistration: aligns the fMRI images with the T1-weighted images. First, FSL's *brain extraction tool (BET)* was applied to both the mean fMRI image and T1-weighted image, to remove the skull. Then, affine registration is performed using

FSL's linear image registration tool (*flirt)*, the resulting transformation matrices (forward and inverse) were saved for the subsequent step.

(5) Normalization: coregisters the T1-weighted image to the standard MNI space. This procedure was implemented in two subsequent steps using FSL tools for affine (*flirt*) and nonlinear (*fnirt*) registration. First, affine registration was used to align the T1 to the MNI152 template with 1 mm resolution. The outputs of this step are the transformed T1 and the transformation matrix, which is used to initialize the nonlinear registration. Next, nonlinear registration is applied to align T1 to the MNI152 template with 2 mm resolution (Figure 13), this is done to refine the alignment and match the resolution of the atlas (i.e, Alvin CSF mask) used in subsequent analyses. The outputs of this final step are the normalized anatomical image, the warp coefficients map (i.e., voxel-wise deformations), and the inverse warp map to allow transformation back to subject's space.

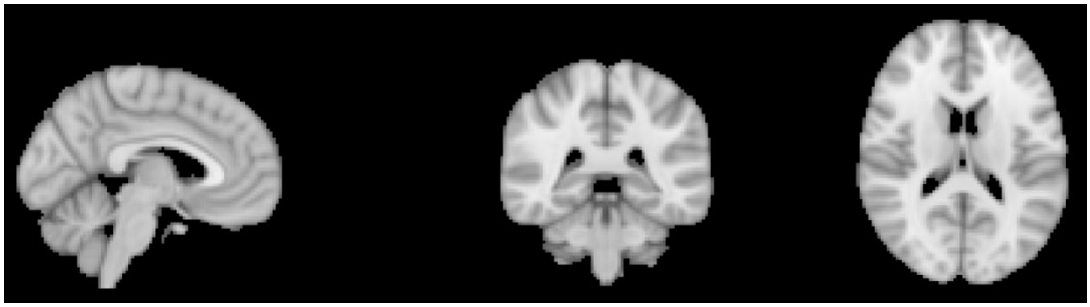

Figure 14. Central slice for MNI152 2mm template

Figure 13. Central slice for 2mm ALVIN CSF mask

(6) Nuisance regression: used to remove sources of noise including low-frequency drifts (<0.01Hz), head motion, and physiological fluctuations. To extract physiological noise components, a cerebrospinal (CSF) mask was created in the functional space. To do this, a CSF atlas (i.e., Alvin CSF mask, Figure 14) defined in the 2mm MNI space, was transformed into subject's anatomical (T1) space using the previously obtained inverse warp field. For each subjects a segmentation of the CSF is done,

obtaining a probabilistic map. Combining the Alvin CSF mask with subject specific CSF and applying a high probability threshold (e.g., 0.99) ensures that only voxels that are highly probable to be CSF are included. To further refine the mask morphological erosion was also applied. The refined CSF was the mapped from the T1 space to fMRI space using previously defined transformation matrix.

Low-frequency drifts were modelled using polynomial regressors. Head motions were modelled using the Friston-24 approach, in which 24 motion parameters are defined upon the 6 rigid body motion parameters. Principal components were extracted from CSF regions defined earlier and used as regressors. Data Processing and Analysis for Brain Imaging (DPABI) MATLAB toolbox was used to regress out these components (*y_RegressOutImgCovariates*).

(7) Filtering: after nuisance regression a temporal ideal bandpass filter (0.008-0.09 Hz) is applied to isolate frequency components of interest and remove slow drifts and high frequency noise. The ideal band-pass filter was implemented using *y_IdealFilter* from the DPABI toolbox. In parallel, the unfiltered data were preserved to allow comparison between preprocessing strategies with or without the use of this band pass filter.

From a theoretical perspective, an ideal bandpass has a rectangular frequency response corresponding to an infinite sinc impulse response in the time domain introducing oscillations over the whole signal. The filter implemented in *y_IdealFilter* applies a rectangular frequency mask in the discrete Fuorier domain, resulting in an abrupt cutoff. Within the *y_IdealFilter* function, input time series are transformed into the frequency domain using Fast Fourier Transform (FFT). The mean of the signal is removed before filtering to remove the DC. Zero-padding is applied to extend the signal length to the next power of two (e.g., initial length N=200, $N_{padded} = 256$) to improve computational efficiency of FFT and to increase frequency resolution without altering the information in the signal. The maximum frequency contained in the BOLD signal is 0.2 Hz, given that sampling frequency is fs = 1/TR = 1/2.5s = 0.4Hz, and according to Nyquist theorem the highest frequency that can be represented without aliasing is $f_s/2$ (i.e., Nyquist frequency). A rectangular frequency mask, with the low cut off frequency at 0.008 Hz and high cut off at 0.09 Hz, was applied to each signal. Within this band the filter has a 0 dB gain, meaning that in theory it maintains the

amplitude of the signal in the passband, while the frequencies outside the passband are suppressed. The filtered signal is then transformed into the time domain using inverse FFT.

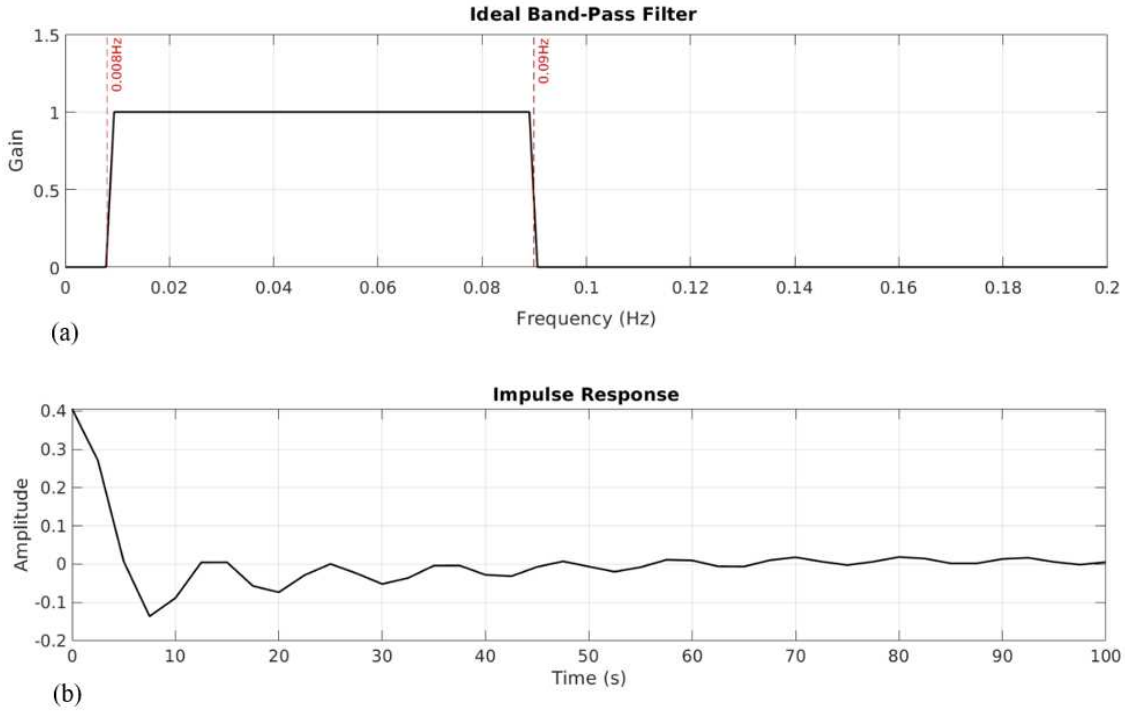

Figure 15. Representation of the band-pass filter implemented in the y_idealFilter function both in frequency domain with the low cut off at 0.008 Hz and high cut off at 0.09 Hz (a) and the corresponding impulse response in the time domain (b).

5.5 Statistical Analysis – GLM

The statistical analysis based on the GLM was performed using SPM12 with the steps specified in MATLAB batch scripts. As explained in the introduction Chapters (2.5 and 3.1) this is done to identify regions with significant task-related activation and plays an important role in VOI extraction for the subsequent DCM analysis. Before GLM, additional processing steps were applied to ensure spatial normalization and to enhance signal quality. Functional images were normalized to the MNI 2mm space using *spm.spatial.normalise* function from matlabbach. Following normalization, images were spatially smoothed with a 6 mm Gaussian kernel using *spm.spatial.smooth* from matlabbatch. The statistical analysis was carried in two steps: first-level analysis and second level analysis. For first-level analysis the GLM was specified through the design matrix definition. Because trials lasted for 3s, a duration inferior to the time constant of the HRF, the trials were modelled as stick functions at the onset times in the experimental paradigm as done in previous studies (Alahmadi et al., 2016; Casiraghi et al., 2019; Lorenzi et al., 2025). Polynomial expansion up to the fourth order, specified by the integral of the grip responses, were used to model linear and nonlinear BOLD responses relative to GF. The 0^{th} order term represents the main effect of hand gripping in comparison to the rest condition, independently of the GF applied. First order expansion models linear changes in the signal with the GF level, and higher order modulations introduce subsequent regressors that account for non-linearity. Stick function encoding grip trials were modulated with the polynomial expansions of GF and convolved with canonical HRFs, thus obtaining the first 5 regressors. Realignment parameters (6 rigid body transformations) obtained from preprocessing were included as regressors of no interest. Low frequency baseline fluctuations were included as the last regressor, for a total of 12 regressors defined. After model specification the model is estimated obtaining the β_{1-12} maps, which contain voxel wise parameter estimates.

Contrast vector, for a T-contrast implementation, is defined as c = [1 0 0 0 0 0 0 0 0 0 0 0] corresponding to the main effect of task versus rest (i.e., first column in the design matrix). Contrast maps were defined as in expression (14). The obtained contrast map for each subject is thus equivalent to the β_1 map, used for second level analysis.

The second-level analysis was performed using the contrast maps from the first-level GLM to identify regions that are activated consistently across subjects. For the group level the designs matrix has only one regressor which represents the mean activation across subjects. In this case t-test is used to determine if the mean activation is significantly different from zero ($H_0: mean\ contrast = 0$) was performed to obtain group SPM{T}, which represent mean group-level activation and is subsequently used for the VOI extraction procedure. Statistical maps were displayed using FSL (FSLeyes), after GLM estimation.

5.6 Visuomotor network

Given the visuomotor nature of the task, the regions involved in this study were selected based on their visuomotor processing assessed by literature and the previous studies performed on the same dataset (Alahmadi et al., 2016; Casiraghi et al., 2019; Lorenzi et al., 2025). Due to the contralateral organization of the motor and sensorimotor systems, cortical regions were defined contralateral to the moving right hand, while the primary visual cortex is involved bilaterally. The cerebellum was defined ipsilaterally, given its ipsilateral motor control. The visuomotor network (Figure 16) includes following regions:

(1) bilateral primary visual cortex (V1), which is involved in many levels of visual analysis such as early feature detection (e.g., edges, orientation and spatial details) and higher order perceptual processing (e.g., object recognition) reflecting more complex visual computations (Lee et al., 1998).

(2) left primary motor cortex (M1), whose fundamental function is the control of voluntary movements, and is interconnected with premotor and supplementary motor areas, as well as the cerebellum forming a network that supports motor execution, adaptation and learning (Sanes & Donoghue, 2026)

(3) left supplementary motor area (SMA) and premotor cortex (PMC), complementarily involved in motor planning, with SMA being more involved in internally generated movements and PMC being involved in movements guided external sensory cues(Roland et al., 1980; Van Oostende et al., 1997).

(4) left cingulate cortex (CC), engaged in multiple functions, including the integration of motor action and outcome information for action-outcome learning, in which actions are

learned to obtain goals based on the outcomes, as well as memory and emotion (Rolls, 2019).

(5) left superior parietal lobule (SPL), is involved in the processing of limb position and monitoring to build complex representations of posture (Felician et al., 2004).

(6) right cerebellum (CRBL), particularly right cerebellar lobule VI, was selected for this study as it is involved in sensorimotor integration, coordination, prediction and motor learning (Prati et al., 2024).

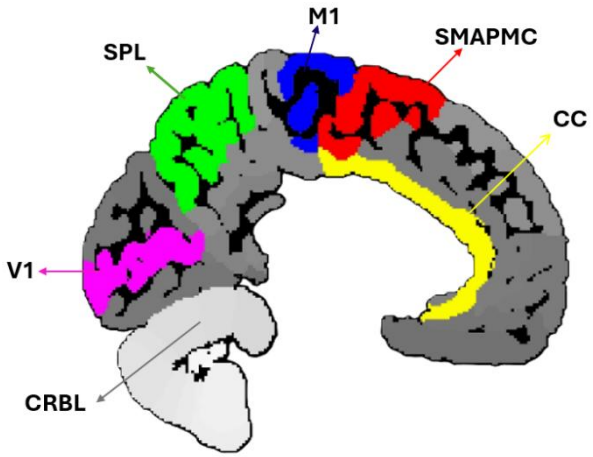

Figure 16. Schematic illustration of brain regions included in the visuomotor network analysed in this study; V1 – Primary visual cortex (magenta), M1 – Primary motor cortex (blue), SMAPMC – Supplementary motor area and Premotor cortex (red), CC – Cingulate cortex (yellow), SPL – Superior parietal lobule (green), CRBL – Cerebellum (light grey).

5.7 VOI extraction

VOI extraction was implemented with the use of SPM12 module (*spm.util.voi*) from MATLAB batch scripts and applied on both filtered and unfiltered cohorts. The VOI extraction is a necessary procedure to obtain representative BOLD signal from the brain regions (V1, SPL, CC, M1, SMAPMC and CRBL) involved in the visuomotor task. The time series extracted represent the measured BOLD signal for the estimation of the effective connectivity in DCM.

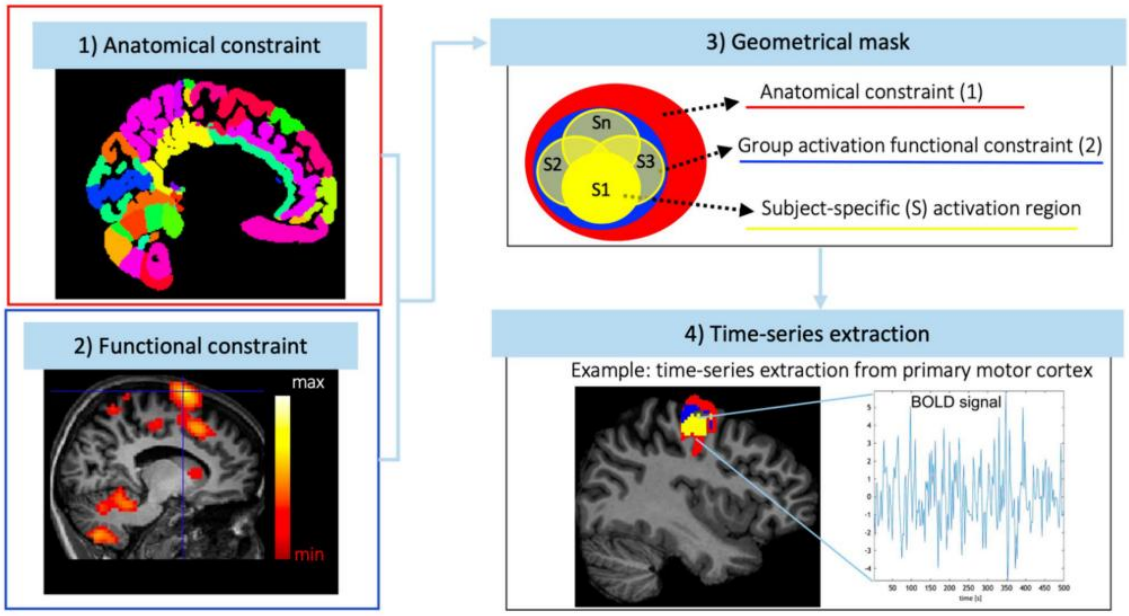

Figure 17. Schematic representation of VOI extraction pipeline. 1) Anatomical constraint defined by anatomical mask extracted for each region from Brodmann and SUIT (for CRBL) atlases. 2) Functional constraint, defined by statistical significance threshold to identify peak activation in each region. 3) Geometrical mask: Box for V1 and different radii spheres for the other regions, with dimensions set according to the anatomical constraint. 4) Time series extraction: Subject specific time series/BOLD signals extracted from geometrical mask centred on activation peak within the region-specific group mask (Lorenzi et al., 2025).

To extract subject-specific VOIs, a group-level VOI extraction was first performed. This step allows the definition of a group activation mask for each region, which will be subsequently used to define the constraint for subject-specific VOI extraction. For each region, group masks were defined as the intersection of anatomical, functional and geometrical constraints. Anatomical constraints (Figure 17.1) used to ensure anatomical plausibility, are defined by adopting the SUIT atlas for the cerebellum and the Broadman (BAM) atlas for the other regions, both defined in 2mm MNI space (Figure 18).

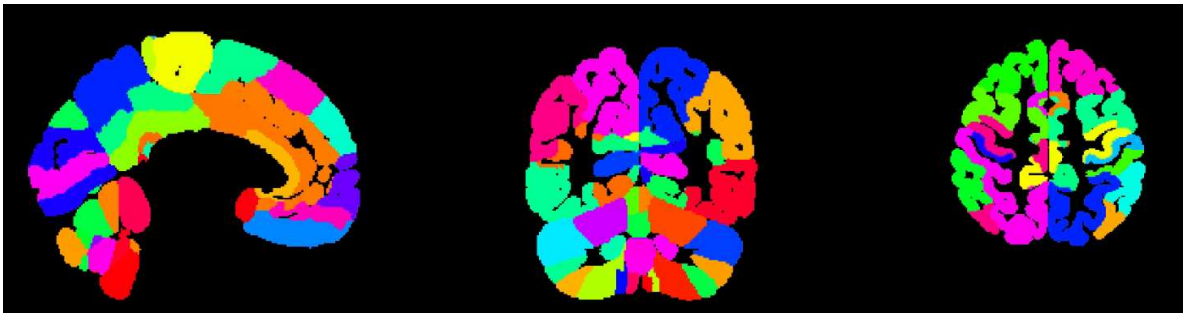

Figure 18. Merged Brodmann and SUIT atlases

The functional constraint (Figure 17.2) is based on the group level task-related activation determined from second-level GLM analysis. It consists of a statistical threshold (e.g, p<0.001) applied on the group SPM{t} map, so voxels that exceed the threshold in terms of T values, are considered active. Geometrical constraints were used to define the extent and the shape of the region around the functional peak within the anatomical region. For V1 geometrical constraint is represented by a box mask of [90 90 90] in units of mm^3. For all the other regions it is a spherical mask of 15 mm radius. The centre of the mask is initialized at [0 0 0] coordinates in MNI space. These initial coordinates are subsequently adjusted at the maximum T value within the anatomical mask, and the geometry is recentred at this activation peak. The intersection of these constraints, determine a binary mask for each region used in the subsequent single-subject VOI extraction.

The subject-level VOI extraction procedure aims to extract time series from single subjects from the same regions of the defined visuomotor network. The extraction procedure is analogous to the one discussed above, where the intersection of constraints defines the region considered to extract representative BOLD signal. Functional constraints were defined by a set of thresholds on the SPM{t} map obtained from first-level GLM analysis. In this case region specific thresholds were applied [V1-0.05, SPL-0.001 CC-0.01 M1-0.001 SMAPMC-0.001 CRBL-0.001]. Group-level masks determined from the group VOI extraction per region are used equivalently to the anatomical constraint defined based on cohort specific mean activations. Geometrical constraints follow an analogous approach adopted for group level VOI extraction. Here the dimension of the geometry is determined upon anatomical considerations. Thus, for V1 the same box constraint [90 90 90] is used, spherical mask of radius 10 mm is used for SPL, CC, SMAPMC, and a 15 mm radius sphere for M1 and CRBL. The intersection of these constraints, determine a binary mask for each region. The first

principal component of the voxels that fall into these defined constraints determine the representative time series. After time series was extracted for both, filtered and unfiltered data, the bandpass filter was applied to the unfiltered data.

5.8 Filter Assessment

5.8.1 Filtering procedure on synthetic signals

In a first investigation of the effectiveness of the filter, synthetic signals were generated, then filtered and analysed both in time and frequency domain. This approach allowed us to verify the filter's ability to preserve in-band frequencies, suppress out-band frequencies, and whether any artifacts are introduced. A first synthetic signal X_1 (Figure 19), was constructed as the sum of sinusoidal components of the same amplitude and placed at representative frequencies of the BOLD time series (i.e., the Slow bands described in Chapter 2.4.1). The components were selected to cover in band and out of band frequencies. The signal was composed of sinusoids at following frequencies $f_{Slow5} = 0.0185\ Hz$ and $f_{Slow4} = 0.05\ Hz$, which are within the passband, and at $f_{Slow3} = 0.135\ Hz$, representing the out of band component. Additionally, two sinusoids were placed on the filter transition frequencies $f_{LOW} = 0.008\ Hz$ and $f_{HIGH} = 0.09\ Hz$, to evaluate behaviour in the transition region.

$$X_1 = \sin(2\pi t f_{LOW}) + \sin(2\pi t f_{Slow5}) + \sin(2\pi f_{Slow4}) + \sin(2\pi f_{HIGH}) + \sin(2\pi f_{Slow3})$$

The constructed signal had N=200 sample points in time, and the same sample frequency used for the real data was defined (fs=0.4Hz), having a total length of 500s, just as the real data.

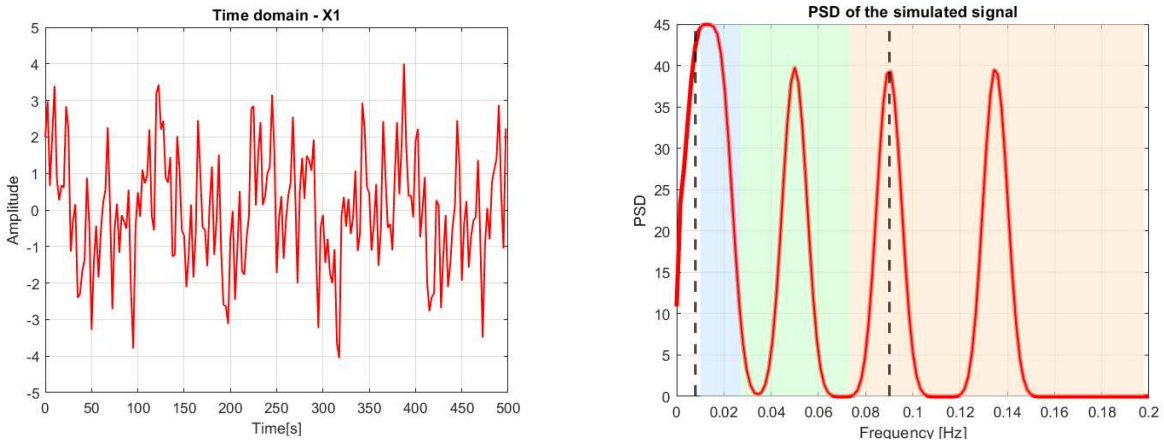

Figure 19. a) Synthetic signal X1 in time domain b) PSD of X1 showing the presence of components in Slow-5(0.01-0.027Hz), Slow-4(0.027-0.073Hz), Slow-3(0.071-0.198Hz) marked respectively by blue, green, and red background; and at transition frequencies marked by vertical dashed lines (0.008-0.09Hz).

Spectral properties of the signal were analysed through the power spectral density (PSD) of the signal. The PSD was estimated using the Welch method, to provide a more robust estimation of the power spectral content by averaging periodograms computed on overlapping bands of the signal. This approach is suggested by (Zuo et al., 2010). In the frequency domain the PSD of the signal were analysed in the passband (0.008-0.09 Hz), Slow-5, Slow-4 and Slow-3 to assess how the filtering changes the power within these bands. The power within specific frequency bands was obtained by integrating the PSD over the studied bands range, allowing to evaluate and compare the energy within the studied bands before and after filtering. Next, loss in decibels (dB) and relative power reduction percentage were computed for a quantitative analysis. Loss in dB evaluates the attenuation of the filtered signal power P_{FILT} relative to the unfiltered signal P_{UNFILT} on a logarithmic scale, and is defined as follows:

$$Loss\ (dB)\ = 10 \log_{10} \frac{P_{FILT}}{P_{UNFILT}} \tag{27}$$

The relative power reduction ($P_{red}\%$) quantifies the relative loss of signal power due to filtering, providing a measure of how much of the original energy is lost:

$$P_{red}\% = \frac{P_{UNFILT} - P_{FILT}}{P_{UNFILT}} \times 100 \tag{28}$$

A second synthetic signal X_2 was implemented to better approximate spectral characteristics of the BOLD signal, including LFOs as well as frequency contributions associated with respiratory (0.1 to 0.5 Hz) and motion noise sources (~ 0.06 Hz aliased) (Cordes et al. 2001, Hallquist et al. 2013). On this second signal a simplified regression procedure was done in MATLAB, to investigate possible interactions between the two procedures, particularly regarding signal distortion and attenuation effects within the passband, as highlighted in previous studies (Hallquist et. al 2013). This allows a controlled evaluation, given that all frequency components in the constructed signals are known.

5.8.2 Application of the filtering procedure to the visuomotor network real data

The VOIs embedded in visuomotor network undergo to three different filtering procedure:

(i) Bandpass filtering: Bandpass filter during the fMRI preprocessing, namely the filter has been applied voxel-wise as last step of fMRI preprocessing and then VOIs were extracted

(ii) No filtering: VOIs were extracted from unfiltered fMRI data (i.e. after step 6 of the preprocessing described in Chapter 5.4)

(iii) Post-extraction filtering: VOIs were extracted as in (ii) and then the filter was applied to the VOIs

This experimental investigation allows to assess whether the temporal filtering alters the spectral content and amplitude of the BOLD signal. The analysis is particularly relevant in the context of DCM, as effects introduced by the filter may affect the modelled fixed effective connectivity.

Qualitative analyses of the timeseries were made both in time-domain and frequency domain, in which the PSD was analysed. To quantify the effects of the filtering, metrics were adopted to evaluate the PSDs from the three cohorts, to make both absolute and relative comparisons. The mean power and standard deviation (SD) were calculated within the considered frequency bands. Loss in decibels (*27*) and relative power reduction (*28*) mentioned for the analysis of the constructed signal (Chapter 5.8.1) were adopted for this analysis.

A paired t-test was performed, to assess if the difference in mean band power between filtered and unfiltered signals is statistically significant. Specifically, paired t-test were performed using the unfiltered condition (ii) as reference, comparing (ii) and (i) and (ii) and (iii). The null hypothesis assumed equal mean power of the conditions compared ($H_0: \bar{P}_{FILT} = \bar{P}_{UNFILT}$), with a significance threshold of $p < 0.05$. In addition to the statistical significance, effect size was computed to evaluate the magnitude of the filtering effect. While p-values indicate the probability of obtaining the results under null hypothesis, effect size provides information on the strength of the effect independent from sample size. Effect size was computed through Cohen's d (29) as the ratio between the mean difference between the unfiltered and filtered signal μ_{diff} and the standard deviation of the difference σ_{diff}.

$$d = \frac{\mu_{diff}}{\sigma_{diff}} \tag{29}$$

The observed effect can be interpreted as small (d=0.2), medium (d=0.5), large (d>0.8) (Brydges, 2019; Cohen, 1988, p. 8)

The metrics were implemented for each subject for each of the three conditions and then mediated across VOIs. To assess the effect of the filter, particularly within the passband, unfiltered condition (ii) was used as reference. The frequency ranges considered for the comparison between (ii) and (i), (ii) and (iii) are passband (0.008 – 0.09 Hz), Slow-5 and Slow-4.

5.9 DCM - Fixed Effective Connectivity Analysis

Fixed effective connectivity within the visuomotor network was investigated through DCM with the use of SPM12 via MATLAB batch scripts, allowing a reproducible pipeline for subjects and all 3 sets of explored data. As explained in the DCM Chapter 3, the method allows the modelling of directed causal interactions and how these are driven by external inputs. In this study the analysis aims to investigate how the preprocessing conditions relative to the bandpass filter application may alter the fixed causal connections estimated by the model.

5.9.1 Models Specification and Estimation

Model specification was identical for all preprocessing conditions (i.e., (ii) unfiltered data, (i) filtered data, and (iii) filtering after VOI extraction), ensuring that eventual differences in parameter estimates and model selection are to be attributed only to the effect of the temporal filtering. To obtain comparable models across subjects, all models were constructed using the same nodes, corresponding to the 6 regions of the visuomotor network (V1, SPL, CC, M1, SMAPMC and CRBL). The experimental driving input u(t), representing the visuomotor task, was modelled as entering the network through V1 for all models and specified through Matrix C. This is justified by the fact that visual cue was presented first. The competing models differed only for their fixed effective connectivity, specified through Matrix A. The alternative connections specified represent the different hypotheses on the directed causal connections within the visuomotor network. Modulatory effects (Matrices B) were not included, as the analysis focused exclusively on the fixed connectivity. In particular, the five competing models (Figure 20) were defined based on previous studies (Casiraghi et al., 2019; Lorenzi et al., 2025), which assessed how information is propagated through cortico-cerebellar pathways considering the nature of the task and the regions activated during the task.

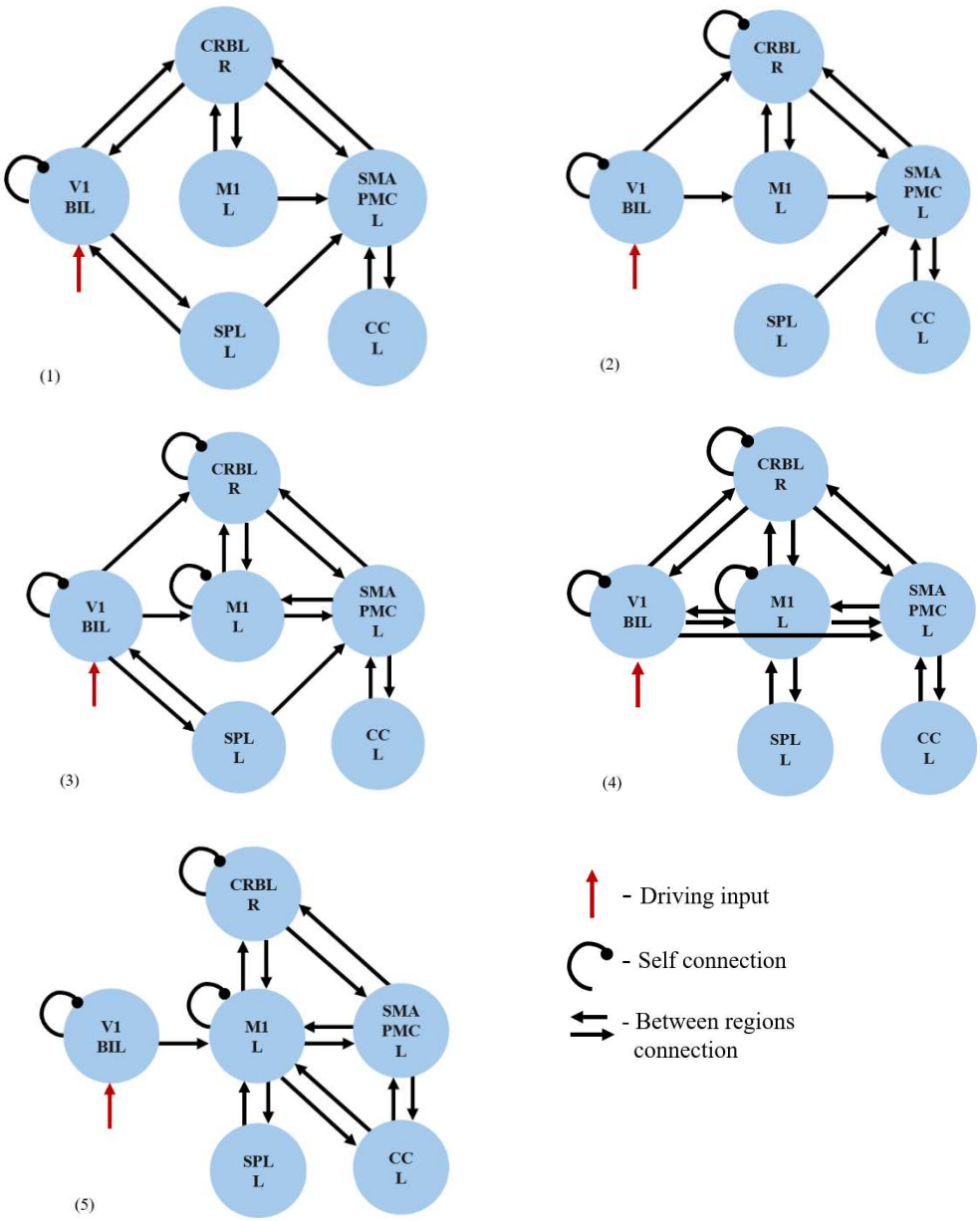

Figure 20. Schematic configuration of five specified models to assess hypotheses on fixed effective connectivity between VOIs, V1 - bilateral primary visual cortex, M1 - left primary motor cortex, CRBL - right cerebellum, SMAPMC - left supplementary motor and premotor cortex, CC - left cingulate cortex, SPL - left superior parietal lobule. The acronym of each region reports also the laterality left (L), right (R), bilateral (BIL).

The direction of the arrows between regions represents the explored causal directed connections. Forward connections in the models represent the propagation of visual information from V1 to motor planning and control areas (SMAPMC and M1), as well as well as CRBL, through visuomotor integration in SPL and CC. Backward connections represent sensorimotor feedback in the cortical-cerebellar loops, accounting for movement correction and prediction. For all models V1 has a recurrent connection (Figure 20).

In Model 1 (Figure 20.1) regions that present bidirectional connections are V1 with CRBL, and SPL, CRBL with V1 and M1 and SMAPMC, CC and SMAPMC. Forward connections are between M1 and SMAPMC and SPL and SMAPMC.

In Model 2 (Figure 20.2), V1 is connected directly to M1 and CRBL. CRBL is self-connected and presents bidirectional connections with M1 and SMAPMC. SPL projects to SMAPMC, without direct connections to M1 or V1 in this model. CC is bidirectionally connected to SMAPMC.

In Model 3 (Figure 20.3), V1 is connected to M1 and CRBL with a forward pathway and has bidirectional connection with SPL, which projects to SMAPMC. CRBL receives the input from V1 and forms a loop through bidirectional connections with both M1 and SMAPMC, which are also reciprocally connected. CRBL and M1 are self-connected. CC is bidirectionally connected to SMAPMC.

In model 4 (Figure 20.4), V1 sends the visual information directly to SMAPMC, and is bidirectionally connected to CRBL and M1. CRBL and M1 are also self-connected. M1 in turn is also bidirectionally connected to V1, SMAPMC, CRBL, and SPL. SMAPMC receivs input form V1 and is bidirectionally connected to CC, CRBL and M1.

In model 5 (Figure 20.5), V1 projects to M1 which is bidirectionally connected to CRBL, SPL, CC, SMAPMC. SMAPMC closes the loop with bidirectional connection to CRBL and CC.

The MATLAB script collects all this information upon model specification in a matrix form. The number of regions (nVOI=6) and experimental conditions are specified to match the GLM design matrix from first-level analysis. Intrinsic connectivity structure for each model was defined through five [6 x 6] A matrices imported from external files. In the matrix, the switched-on connections (i.e., value=1 in the matrix) encode the presence of directional connection between regions and the absence of connection is noted by zero values. The switched off connections are fixed to their prior values and are not updated in Bayesian model inversion. Self-connections are on the diagonal and allowed the investigation of the sensitivity of the region to the input. Matrix C has only one switched on connection relative to V1. For each subject the SPM.mat from first-level GLM analysis is loaded, as it contains the design matrix needed for DCM. All the time series extracted from the VOI extraction

procedure are also loaded, with each subject having a total of 6 times series from the corresponding VOI. Model specification was performed using SPMs function defined in MATLAB *spm_dcm_specify*. Model estimation was performed using *spm_dcm_estimate*, which applies Bayesian model inversion and estimates the effective connectivity parameters and computes the model evidence. After estimation models were grouped to proceed with second-level analysis. The five models were specified and implemented for all three preprocessing conditions.

5.9.2 Bayesian Model Selection and Bayesian Model Averaging

To identify which of the five models tested better explains the observed data, BMS was performed. This approach allows the comparison of the different hypotheses by evaluating their model evidence as explained in Chapter 3.3. Particularly the RFX approach, which accounts for variability between subjects, was used adopting the PEP metric.

After the most likely model has been found, BMA was implemented to infer the winning model at group-level. BMA was implemented by using *spm_dcm_bma* obtaining the average over the subject specific parameters. To illustrate the posterior probabilities on the strength of connections for all the datasets under study, heatmaps were used. This procedure was done for the three preprocessing conditions (i.e., (ii) unfiltered, (i) bandpass filtered, (iii) filtered after VOI extraction) to assess whether the filtering procedure changes the fixed effects connectivity. Pairwise t-test were performed to compare fixed connectivity parameters obtained under conditions (i) and (iii) to the unfiltered reference condition (ii). The null hypothesis under test was that there are no significant differences in the fixed estimated connectivity parameters between conditions, with statistical significance set for $p < 0.05$.

6. Results

6.1 Preprocessing

The preprocessing pipeline was applied to all 21 subjects. Two datasets were obtained, the unfiltered data was obtained by omitting the bandpass filtering steps, the filtered data by applying the filter. Visual inspection of the fMRI images and mean fMRI did not reveal appreciable differences between the two conditions. As shown in Figure 21, mean images from unfiltered and filtered datasets appear visually very similar. Additionally, the mean fMRI images confirm the correct application of preprocessing steps (realignment, coregistration, normalization), as reflected by the consistent positioning, shape and scale of anatomical structures across subjects and conditions.

a.

b.

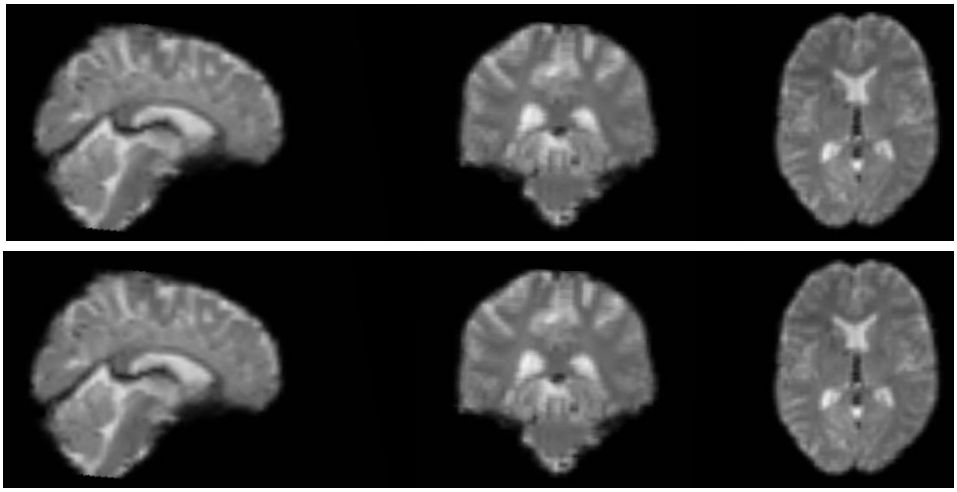

Figure 21. Mean fMRI images of a random subject a) Unfiltered b) Filtered before VOI extraction, conditions

6.2 Statistical Analysis – GLM

Statistical maps were obtained from the GLM analysis described in Material and Methods (Chapter 5.5) for the unfiltered and bandpass filtered data of 21 subjects. Where subject specific contrasts, representing the main effect of the task, were computed and used for the second level analysis to identify group activations, and subsequently used for the VOI extraction procedure. At subject level, SPM{T} maps presented clear differences between preprocessing conditions (ii) and (i). In the unfiltered condition (ii), SPM{T} maps show more intense and larger number of statistically significant voxel ($p<0.001$). In the bandpass

filtered data, resulting SPM{T} maps show a reduction in intensity and activation extent. These differences can be observed in Figure 23Figure 22 , with SPM{T} maps of a random subject in unfiltered (ii) (Figure 22.a) and filtered conditions (i) (Figure 22.b).

a.

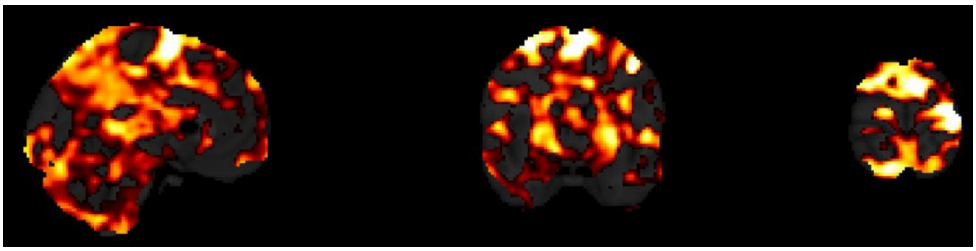

b.

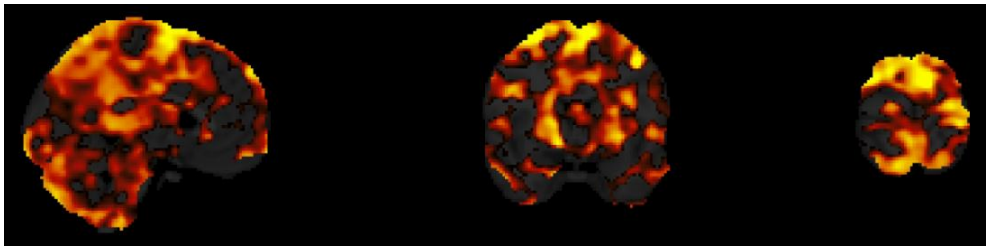

Figure 22. SPM{T} maps of a random Subject in a) Unfiltered (i) b) Filtered before VOI extraction, conditions (i).

Similarly at the group level, activations appear more extended and intense in the unfiltered condition (ii) (Figure 23.a). In the filtered condition (i), activations result to be spatially reduced with less intense clusters, particularly in regions such as V1 and CRBL. This results overall show a reduction of significantly active voxels considering the same threshold ($p<0.001$), both a subject and group level.

a.

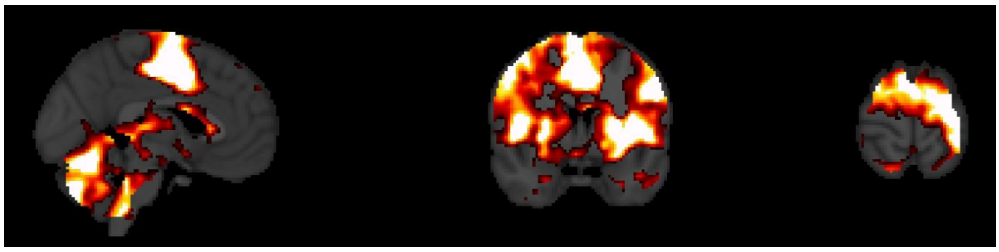

b.

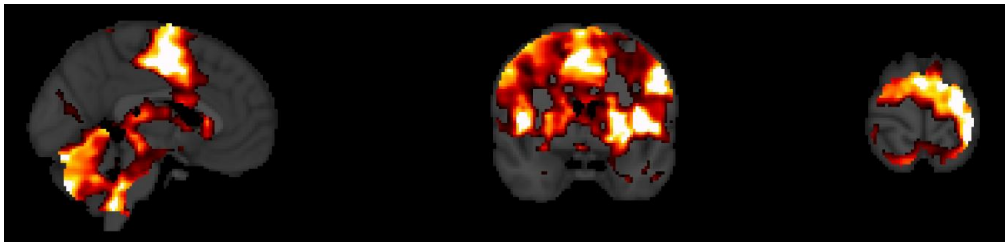

Figure 23. Group SPM {T} a) Unfiltered b) Filtered before VOI extraction, conditions

6.3 VOI extraction

VOI extraction procedure was successfully completed for all 21 subjects and all VOIs in the unfiltered data, resulting in 6 time series per subject, one for each region of the visuomotor network. All selected VOIs showed significant activation at subject level, according to statistical thresholds used (Chapter 5.7). For the filtered dataset (condition i), VOI extraction resulted incomplete. All 6 VOIs were extracted only for 14 subjects, while in the remaining 7 subjects one or more VOIs did not reach statistical significance. Among the 7 subjects with the incomplete network, the most frequently missing regions were CRBL for 4 out of 7 subjects, followed by V1 for 3 subjects, SMAPMC and SPL for one subject.

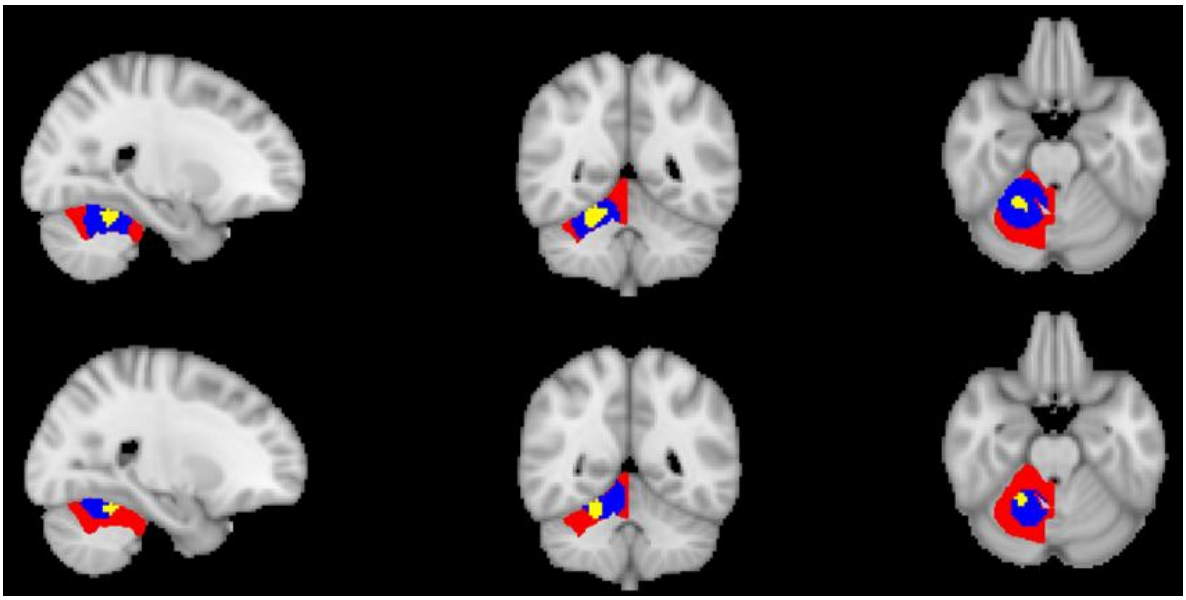

Figure 24. Example of VOI extraction for the cerebellum (CRBL) in a random subject under two preprocessing conditions: Unfiltered (top), Filtered before VOI extraction (bottom). With subject specific time series extracted considering the conjunction of constraints anatomical (red), group activation (blue), subject specific activation (yellow) masks.

A systematic reduction in the spatial extent of VOIs extracted in the filtered condition (i) was observed compared to the unfiltered one (ii). Particularly, both group-level and subject-specific activation masks appeared reduced. An example of the overlapping constraints for the time series extraction from CRBL in a random subject, is shown in Figure 24 for the unfiltered condition and filtered before VOI extraction, where the reduction of group-level (blue) and subject specific (yellow) activation masks can be observed.

6.4 Filter Assessment

6.4.1 Filtering procedure on synthetic signals

The synthetic signal X1, composed of known frequencies described in Material and Methods (Chapter 5.8.1), can be observed in the time domain and frequency domain before and after filtering in Figure 25. In the time domain (Figure 25.a) the filtered signal preserves the unfiltered signal structure, while showing a reduction in high fluctuations. The PSD of the filtered signal represented in green in (Figure 25.b) shows that the component outside the passband (0.135 Hz) is suppressed. Components near transition frequencies are attenuated, while the component in the middle of the band is preserved.

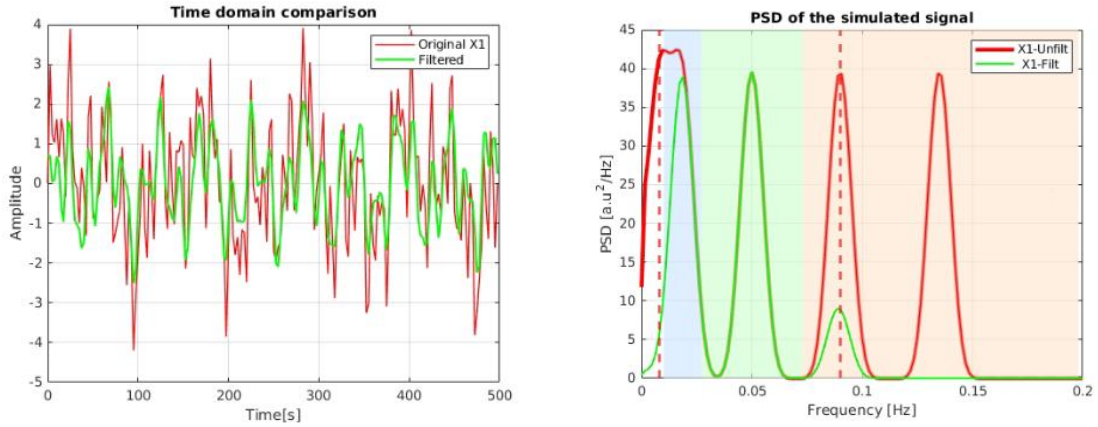

Figure 25. a) Time domain Original X1 signal (red) and Filtered X1 (green). b) PSD of the original X1(red) and band pass filtered X1 (green), backgroung shows the portion of Slow-5(0.01-0.027Hz), Slow-4(0.027-0.073Hz), Slow-3(0.071-0.198Hz) bands marked respectively by blue, green, and red shades; transition frequencies are marked by vertical dashed lines (0.008-0.09Hz).

Within the passband the relative power reduction is 23.9% corresponding to a 1.18 dB loss. Considering the subdivision in Slow bands ranges, the relative power reduction in Slow-5 band is of 20.5% corresponding to a 1 dB loss, for Slow-4 the relative power reduction is of 0.12% corresponding to a 0.01 dB loss. The component within the Slow-3 band has a relative power reduction of 89.6% corresponding to a 9.59 dB loss. With filter successfully attenuating the components outside the passband and, within the passband showing a more prominent reduction in Slow-5 with rather than Slow-4.

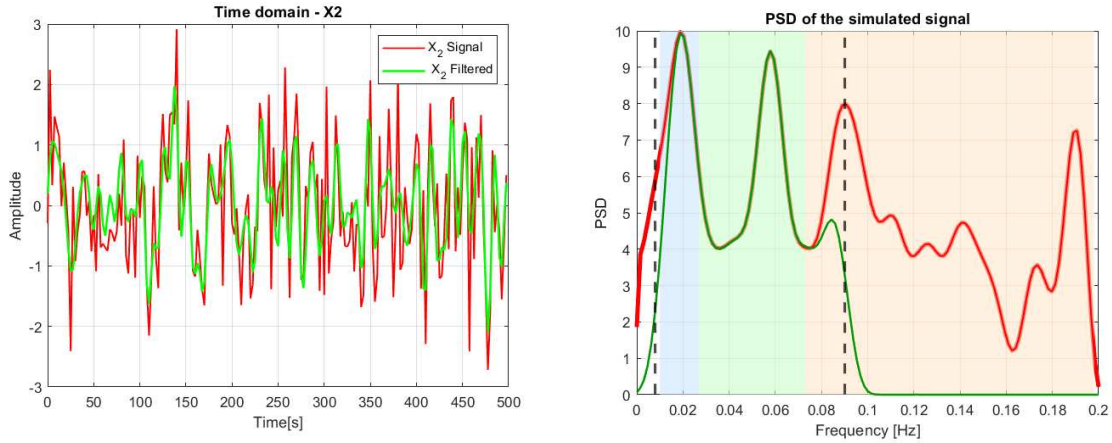

a. b.

Figure 26. a) Time domain Original BOLD like X2 signal (red) and Filtered X2 (green). b) PSD of the original BOLD like X2(red) and band pass filtered X2 (green); backgroung shows the portion of Slow-5(0.01-0.027Hz), Slow-4(0.027-0.073Hz), Slow-3(0.071-0.198Hz) bands marked respectively by blue, green, and red shades; transition frequencies are marked by vertical dashed lines (0.008-0.09Hz).

For the X2 constructed signal, which is more BOLD like (Figure 26.a), in the time domain high frequency peaks appear to be more reduced, with the filtered signal preserving the overall signal structure, similarly to the X1 synthetic signal. In the frequency domain (Figure 26.b), for the passband the relative power reduction is 6.28% corresponding to a 0.28 dB loss. Within the passband, for the Slow-5 the relative power reduction is of 5.37% corresponding to 0.24 dB loss, for the Slow-4 the relative power reduction is of 0.02 % which corresponds to a near null dB loss. Slow-3 is reduced by 84.62%, which corresponds to a loss of 8.13 dB. As for X1, components near transition frequencies are attenuated (Figure 26.b). Although both X1 and X2 contain components near the passband transition frequencies, X2 has a greater proportion of in band (0.008-0.09 Hz) power, resulting in a more preserved signal. Constructed physiological noise spread across the X2 signal were successfully regressed out without interfering with the filtering procedure.

6.4.2 Application of the filtering procedure to the visuomotor network

Time series extracted from the VOIs were compared across the three filtering conditions, as described in Materials and Methods (Chapter 5.8.2). The comparison was restricted to the 14 subjects, for which all VOIs (CC, CRBL, M1, SMAPMC, SPL and V1) were successfully extracted in condition (i) and performed on the corresponding data of the same subjects under condition (ii) and (iii). The same qualitative temporal behaviour was observed across all subjects. For visualization, the time series of a random subject is shown in Figure 27 for all six VOIs. Across all VOIs, the unfiltered signals (red) show larger amplitude fluctuations, and the presence of rapid oscillations is evident. For conditions (i) and (iii), respectively green and black (Figure 27), it is possible to qualitatively appreciate that time series appear smoother, with reduced signal amplitude and high frequency oscillations. The post extraction and before extraction filtering conditions show similar temporal profiles, preserving the main oscillations patterns at lower frequencies. However, the post extraction signal (black) appears to be slightly smoother with respect to condition (i) in green.

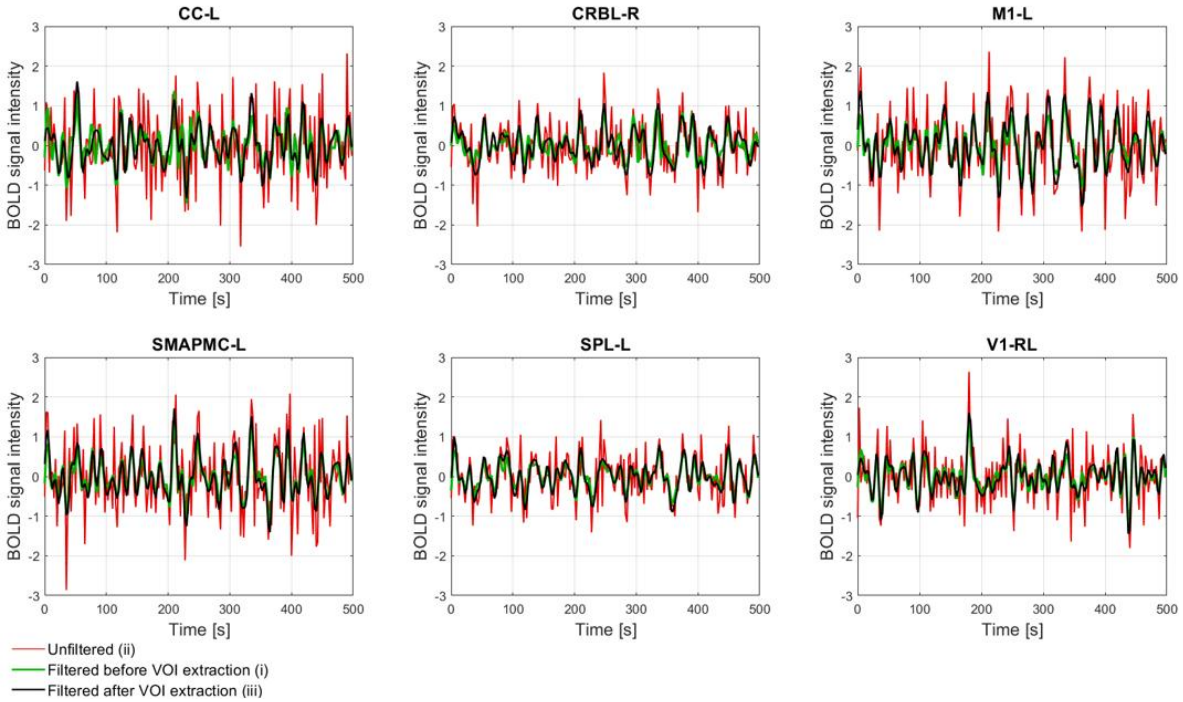

Figure 27. Time series for all VOIs of a random subject for the corresponding filtering conditions: i) Filtered before VOI extraction (green), ii) Unfiltered (red), iii) Filtered after VOI extraction (black). VOIs: V1 - bilateral primary visual cortex, M1 - left primary motor cortex, CRBL - right cerebellum, SMAPMC - left supplementary motor and premotor cortex, CC - left cingulate cortex, SPL - left superior parietal lobule. The acronym of each region reports also the laterality left (L), right (R), bilateral (RL).

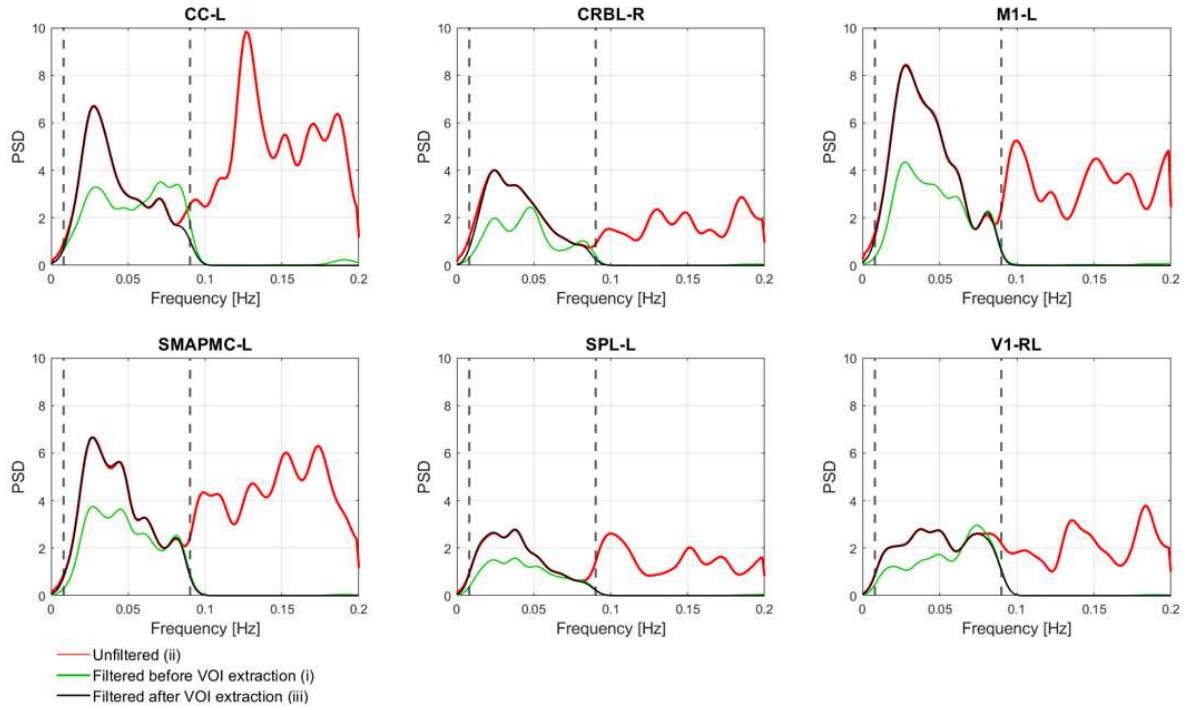

Figure 28. Random subject PSDs for the corresponding filtering conditions: i) Filtered before VOI extraction (green), ii) Unfiltered(red), iii) Filtered after VOI extraction(black); for all VOIs: V1 - bilateral primary visual cortex, M1 - left primary motor cortex, CRBL - right cerebellum, SMAPMC - left supplementary motor and premotor cortex, CC - left cingulate cortex, SPL - left superior parietal lobule. The acronym of each region reports also the laterality left (L), right (R), bilateral (RL).

The PSD of the VOIs' time series was also compared across the three conditions as described in Materials and Methods (Chapter 5.8.2). The analysis over the three conditions was performed on the same subset of 14 subjects as described for the temporal analysis, and the PSD of the same subject selected for the temporal representation is shown in Figure 28. Across all VOIs, the unfiltered signal (red) has power distributed over the entire frequency range, with components above 0.1 Hz. Considering the filtering conditions (i) and (iii) (example in Figure 28), reduction of power is observed outside the passband. The signals filtered after VOI extraction (black) generally show a sharp attenuation outside the cut off frequencies, while maintaining the spectral content and amplitude within the passband. The signals filtered before VOI extraction also show a power attenuation outside the passband, however there are residual components above the higher cut off frequency. Within the passband the power attenuation in condition (i) is more pronounced for some regions with a larger variability in the signal amplitude with respect to condition (iii).

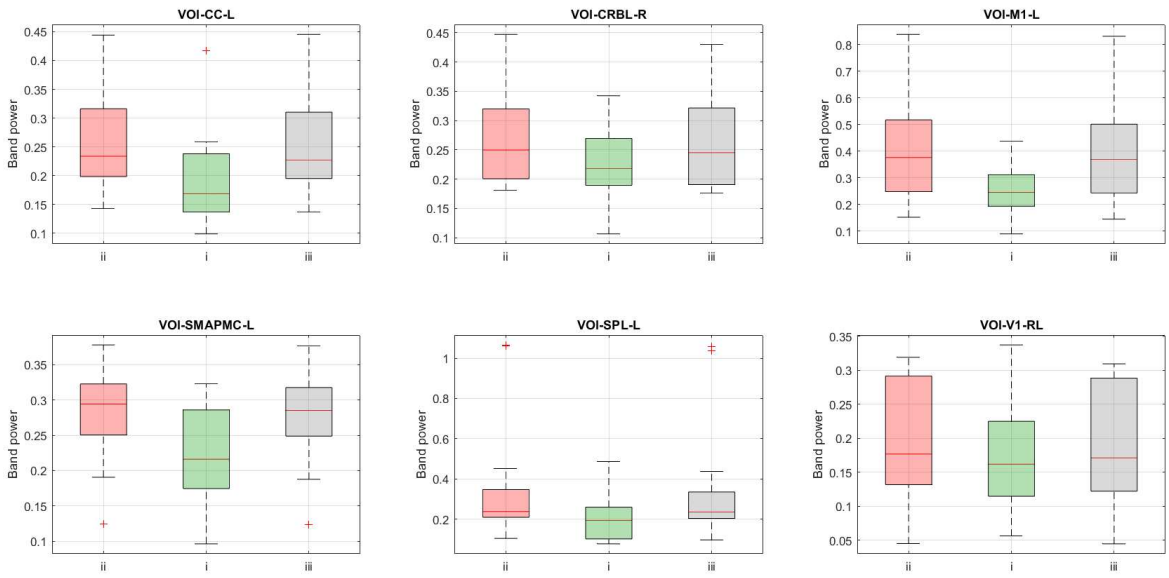

Figure 29. Boxplots of power distribution across all VOIs for 14 subjects, under three preprocessing conditions i) Filtered before VOI extraction(green), ii) Unfiltered(red), iii) Filtered after VOI extraction(grey); VOIs: V1 - bilateral primary visual cortex, M1 - left primary motor cortex, CRBL - right cerebellum, SMAPMC - left supplementary motor and premotor cortex, CC - left cingulate cortex, SPL - left superior parietal lobule. The acronym of each region reports also the laterality left (L), right (R), bilateral (RL).

To assess the effect of the filter within the passband (0.008-0.09 Hz), boxplots (Figure 29) were implemented for each VOI, displaying the power distribution across the three conditions for the subset of 14 subjects. Across all VOIs, the filtering condition (i) shows a systematic reduction in the median band power with respect to the unfiltered data. The decrease is more pronounced in M1 and SMAPMC. The variability is reduced for M1, V1, CRBL and CC, while SMAPMC and SPL show greater variability. For the filtering condition (iii), the impact on the band power is more reduced for all VOIs, as median values do not show a pronounced change in amplitude. Variability of condition (iii) remains similar to the unfiltered condition.

Table 2. Metrics across regions in within the passband (0.008 – 0.09 Hz) analysis, for i) Filtering before VOI extraction and ii) Unfiltered signals.

ROI	*Unfiltered (condition ii) Mean Power ± SD*	*Filtered (condition i) Mean Power ± SD*	*Mean Power Loss [dB]*	*Mean Power Reduction [%]*	*Effect Size - d*	*p-values*
CC	*0.259 ± 0.008*	*0.194 ± 0.007*	*1.34*	*25.24*	*1.6*	*<0.001*
CRBL	*0.272 ± 0.008*	*0.225 ± 0.004*	*0.82*	*14.43*	*0.7*	*0.021*
M1	*0.400 ± 0.036*	*0.254 ± 0.009*	*1.82*	*32.50*	*1.3*	*<0.001*
SMAPMC	*0.282 ± 0.005*	*0.222 ± 0.004*	*1.11*	*20.95*	*1.3*	*<0.001*
SPL	*0.357 ± 0.098*	*0.202 ± 0.012*	*1.91*	*26.65*	*0.5*	*0.074*
V1	*0.204 ± 0.008*	*0.171 ± 0.006*	*0.59*	*12.62*	*0.7*	*0.017*

Metrics described in the Material and Methods (5.8.2), were computed for a pairwise comparison of power within the passband, between condition (ii) and (i), and between (ii) and (iii), using the unfiltered condition (ii) as a reference. Metrics were first computed for each subject and then mediated for each VOI. Results for the comparison between conditions (ii) and (i), within the passband, are shown in Table 2. For condition (i) the average power is systematically attenuated with respect to the unfiltered condition, and reduction in variability is observed for all regions. The strongest effects are observed in regions M1, SMAPMC and CC. The largest mean power reduction (32.5%) is in M1, corresponding to a mean power loss of 1.82dB, with a large effect size (d = 1.3) and highly significant p-value. CC shows a mean power reduction of 25.24% (-1.34dB), associated with the highest effect size among the VOIs (d = 1.6) and highly significant p-value. Similar effects are observed on SMAPMC, with a mean reduction of 20.95% (-1.11 dB), a large effects size (1.3), and high statistical significance. Effects are more moderate, but still significant, on CRBL and V1. In CRBL, mean power reduction is 14.43% (-0.82 dB), with a significant p-value ($p < 0.05$), and a medium effect size (0.7). In a similar way, V1 shows a reduction of 12.62% (-0.59 dB) and a significant p-value ($p < 0.05$). SPL shows a mean power reduction of 26.65%, and highest power loss across regions (1.91dB) while not presenting statistical significance ($p > 0.05$). This is coherent with a higher power variability across subjects in the SPL both in the filtered condition (i) and unfiltered (ii).

Table 3. Metrics across regions in within the passband (0.008 – 0.09 Hz) analysis, for iii) Filtering after VOI extraction and ii) Unfiltered signal.

ROI	*Unfiltered (condition ii) Mean Power ± SD*	*Filtered (condition iii) Mean Power ± SD*	*Mean Power Loss [dB]*	*Mean Power Reduction [%]*	*Effect Size*	*p-values*
CC	0.259 ± 0.008	*0.253* ± 0.008	*0.11*	*2.46*	*1.3*	*<0.001*
CRBL	0.272± 0.008	*0.265* ± 0.007	*0.13*	*2.86*	*1.5*	*<0.001*
M1	0.400± 0.036	*0.392* ± 0.036	*0.11*	*2.43*	*2.3*	*<0.001*
SMAPMC	0.282± 0.005	*0.277* ± 0.005	*0.09*	*1.99*	*1.4*	*<0.001*
SPL	0.357± 0.098	*0.349* ± 0.096	*0.12*	*2.60*	*1.3*	*<0.001*
V1	0.204± 0.008	*0.198* ± 0.008	*0.12*	*2.75*	*1.5*	*<0.001*

The results of the comparison between condition (ii) and (iii) relative to the within passband power are reported in Table 3. The same procedure as for the previous comparison was applied. Across all VOIs, the mean reduction of power is limited, ranging from ∼2% and 2.9%, corresponding to a mean power loss of approximately 0.09-0.13 dB. For this condition CRBL and V1 present the largest relative reductions of 2.86% (-0.13 dB) and 2.75% (-0.12 dB) respectively, followed by SPL (2.60% and -0.1154 dB), CC (2.46% and -0.11 dB), M1 (2.43% and -0.11 dB) and SMAPMC (1.99% and -0.09 dB). All regions show statistically significant differences between condition (ii) and (iii). With effects sizes being relatively large across VOIs, ranging from 1.3 (CC) to 2.3 (M1), thus describing a systematic effect across subjects. Filtering after VOI extraction produces minimal attenuation within band power, while maintaining a consistent effect across subjects. This condition better preserves the signal with respect to condition (i), although reduction is systematic and present across all regions.

Following the same approach adopted for the passband analysis, to investigate the effect of filtering conditions on the specific low frequency components within the passband, the analysis was extended to the slow bands (described in Chapter 2.4.1). The PSD distribution for each region of a random subject, where slow bands are highlighted, are shown in Figure 30. A marked effect of filtering in both conditions (i) and (iii) is observed in the Slow-3 band, where spectral power is strongly attenuated. In the unfiltered condition, this band frequently included dominant peaks, particularly for CC (9/14 subjects) and V1 (8/14 subjects). Across regions dominant peaks were consistently located within the passband for the M1 (14/14 subjects), and predominantly within the passband for SMAPMC (12/14 subjects), in SPL

(11/14 subjects), and in CRBL for (8/14 subjects). Considering the power distribution across the three conditions, the peaks were mainly within the Slow-4 band for M1, SMAPMC, CRBL and SPL. The Slow-5 bands generally showed a minor contribution in all conditions, although slightly higher relative power was observed in CRBL, SMAPMC, CC and SPL.

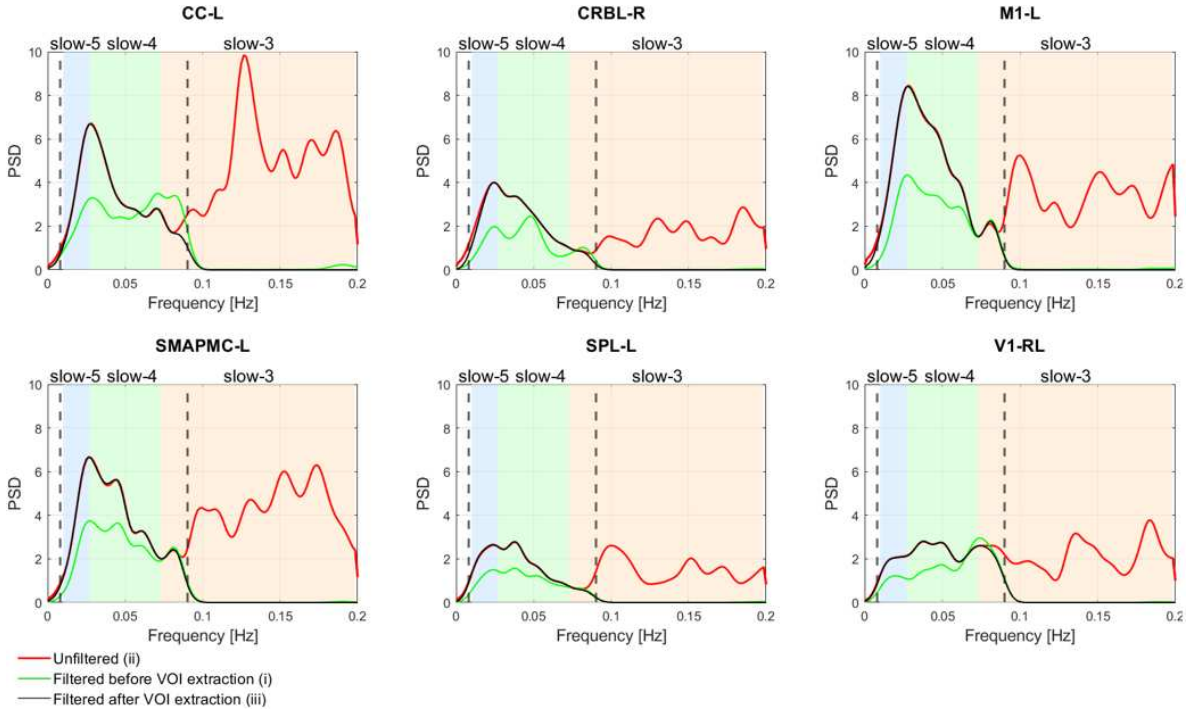

Figure 30. Random subject PSDs across all VOIs for the filtering conditions: i) Filtered before VOI extraction (green), ii) Unfiltered(red), iii) Filtered after VOI extraction(black); The frequency axis is divided into three bands: slow-5, slow-4, and slow-3, highlighted by respectively blue, green, red backgrounds. VOIs: V1 - bilateral primary visual cortex, M1 - left primary motor cortex, CRBL - right cerebellum, SMAPMC - left supplementary motor and premotor cortex, CC - left ùcingulate cortex, SPL - left superior parietal lobule. The acronym of each region reports also the laterality left (L), right (R), bilateral (RL).

When extending the analysis to the full set of 21 unfiltered subjects with all regions extracted, similar trends were observed.

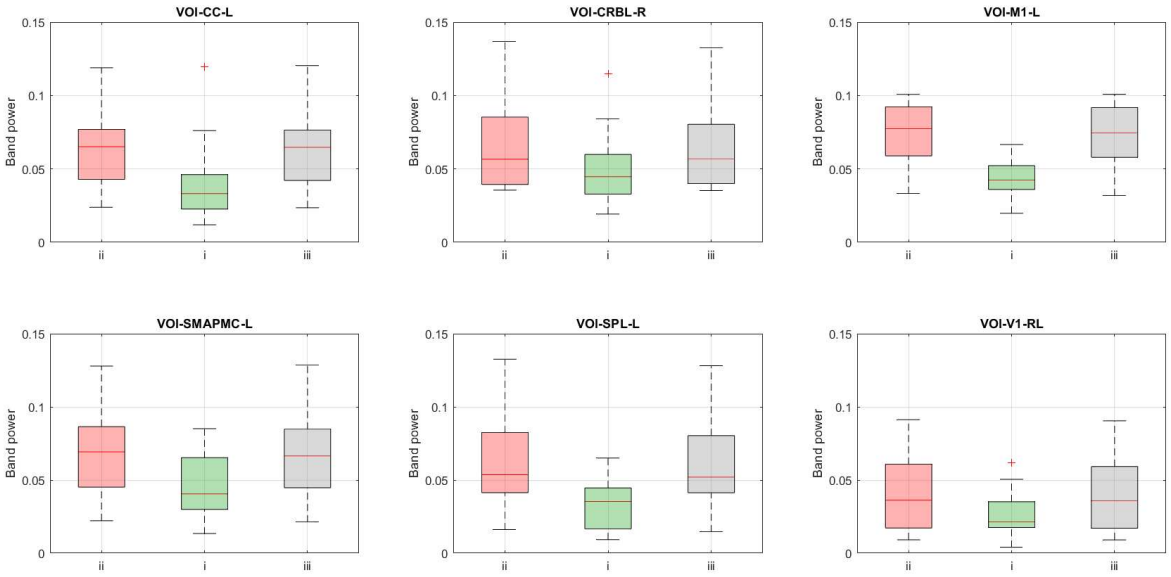

Figure 31. Boxplots for all VOIs analysed in the Slow-5 (0.01 - 0.027Hz) band across under three preprocessing conditions i) filtered before VOI extraction(green), ii) unfiltered(red), iii) filtered after VOI extraction(grey); VOIs: V1 - bilateral primary visual cortex, M1 - left primary motor cortex, CRBL - right cerebellum, SMAPMC - left supplementary motor and premotor cortex, CC - left cingulate cortex, SPL - left superior parietal lobule. The acronym of each region reports also the laterality left (L), right (R), bilateral (RL).

Boxplots for each VOI were used to visualize the distribution of band power across subjects and conditions. In Figure 31 boxplots relative to Slow-5 are shown. Across all regions, relatively low band-power values are observed, with V1 showing the lowest median values. The filtered condition (i) shows consistently a lower median band power compared to both conditions (ii) and (iii) and generally shows a reduced inter subject variability with respect the unfiltered condition. Conditions (ii) and (iii) display similar distributions, having comparable interquartile ranges and median values across regions.

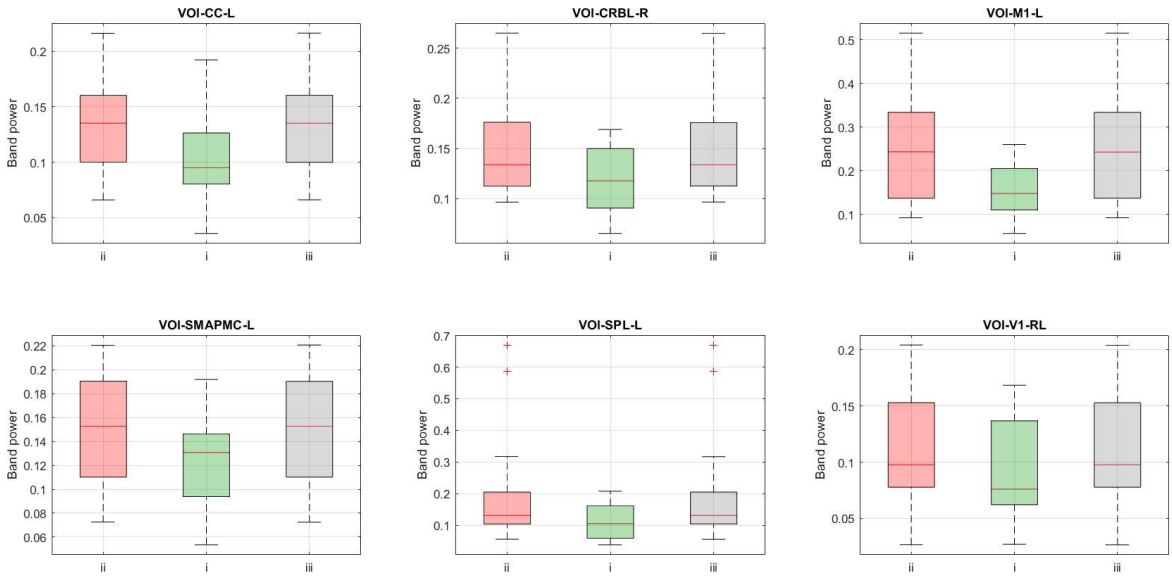

Figure 32. Boxplots of power distribution across all VOIs for 14 subjects within the Slow-4 (0.027-0.073Hz)band band across under three preprocessing conditions i) filtered before VOI extraction(green), ii) unfiltered(red), iii) filtered after VOI extraction(grey); VOIs: V1 - bilateral primary visual cortex, M1 - left primary motor cortex, CRBL - right cerebellum, SMAPMC - left supplementary motor and premotor cortex, CC - left cingulate cortex, SPL - left superior parietal lobule. The acronym of each region reports also the laterality left (L), right (R), bilateral (RL).

Figure 32 shows the boxplots for Slow-4 band. Compared to Slow-5, regions have higher median band power values. Across all VOIs, condition (i) shows a systematic reduction of power compared to condition (ii). Conditions (ii) and (iii) present similar distributions with comparable interquartile ranges and median values across all VOIs.

Table 4. Slow-5 metrics across 14 subjects in condition (i) Filtered before VOI extraction, compared to condition (ii) Unfiltered

ROI	*Unfiltered (condition ii) Mean Power ± SD*	*Filtered (condition i) Mean Power ± SD*	*Mean Power Loss [dB]*	*Mean Power Reduction [%]*	*Effect Size - d*	*p-values*
CC	*0.068 ± 0.001*	*0.041 ±0.0009*	*2.59*	*41.96*	*1.8*	*<0.001*
CRBL	*0.066 ± 0.0008*	*0.049 ±0.0007*	*1.39*	*21.62*	*0.9*	*0.006*
M1	*0.077 ± 0.001*	*0.044 ±0.0002*	*2.29*	*37.23*	*1.2*	*<0.001*
SMAPMC	*0.070 ± 0.0008*	*0.045 ±0.0005*	*1.98*	*33.20*	*1.2*	*<0.001*
SPL	*0.086 ± 0.006*	*0.045 ±0.0029*	*2.93*	*38.48*	*0.5*	*0.088*
V1	*0.042 ±0.001*	*0.027 ±0.0002*	*1.78*	*27.99*	*1.1*	*0.001*

Results regarding the effect of filtering in condition (i) compared to condition (ii) on the Slow-5 frequency band across VOIs are shown in Table 4. The overall quantitative analysis within Slow-5 band shows a pronounced attenuation when filtering is applied before VOI extraction. Across all VOIs the mean power reduction ranges from 21.6% (CRBL) to 41.96%

(CC). Attenuation is significant for all regions except SPL ($p > 0.05$), which despite having a mean power reduction of 38.5% (-2.9 dB) has a higher variability across subjects reducing statistical significance. Larger effect size and significance is observed for CC, M1 and SMAPMC corresponding to a mean power loss between approximately 2 and 2.6 dB. V1 and CRBL show lower reduction in Slow-5 but still presenting a significant difference ($p<0.05$).

Table 5. Slow-4 metrics across 14 subjects in condition i) Filtered before VOI extraction, compared to condition ii) Unfiltered

ROI	*Unfiltered (condition ii) Mean Power ± SD*	*Filtered (condition i) Mean Power ± SD*	*Mean Power Loss [dB]*	*Mean Power Reduction [%]*	*Effect Size - d*	*p-values*
CC	*0.131 ± 0.019*	*0.102 ± 0.002*	*1.17*	*21.72*	*1.2*	*<0.001*
CRBL	*0.149 ± 0.002*	*0.121 ± 0.001*	*0.88*	*15.73*	*0.8*	*0.015*
M1	*0.250 ± 0.018*	*0.156 ± 0.004*	*1.83*	*32.42*	*1.2*	*<0.001*
SMAPMC	*0.154 ± 0.020*	*0.124 ± 0.002*	*0.98*	*18.99*	*1.2*	*<0.001*
SPL	*0.208 ± 0.040*	*0.115 ± 0.003*	*1.87*	*24.44*	*0.5*	*0.073*
V1	*0.109 ± 0.002*	*0.092 ± 0.002*	*0.70*	*13.66*	*0.8*	*0.009*

Results regarding Slow-4 band across 14 subjects comparing conditions (ii) and (i) are shown in Table 5. Mean power for the two compared conditions is higher in the Slow-4 band with respect to Slow-5. The mean power reduction and mean power loss within Slow-4 are lower compared to ones observed in the Slow-5 band but maintain a similar overall behaviour. The mean power reduction ranges between 13.7% (V1) and 32.4% (M1). Largest attenuation is observed in M1, followed by SPL (24.4%) and CC (21.7%), corresponding to a power loss between 1.17 and 1.87 dB. Larger effect sizes are observed for M1, SMAPMC and CC, reflecting the statistically significant differences between the two conditions. CRBL and V1 also show statistically significant differences ($p < 0.05$), although with smaller effect sizes, thus having a less pronounced attenuation. Similarly to previous observations, SPL does not reach statical significance ($p > 0.05$).

Table 6. Slow-5 across 14 subjects in condition iii) Filtered after VOI extraction, compared to condition ii) Unfiltered

ROI	*Unfiltered (condition ii) Mean Power ± SD*	*Filtered (condition iii) Mean Power ± SD*	*Mean Power Loss [dB]*	*Mean Power Reduction [%]*	*Effect Size - d*	*p-values*
CC	*0.068 ± 0.001*	*0.067 ±0.001*	*0.0768*	*1.71*	*0.6*	*0.056*
CRBL	*0.066 ±0.0009*	*0.066 ±0.0009*	*0.0568*	*1.28*	*0.6*	*0.060*
M1	*0.077 ±0.0009*	*0.076 ±0.0009*	*0.0637*	*1.44*	*0.8*	*0.014*
SMAPMC	*0.069 ±0.0008*	*0.068 ±0.0008*	*0.0746*	*1.68*	*0.7*	*0.027*
SPL	*0.086 ±0.0066*	*0.040 ±0.0065*	*0.1084*	*2.42*	*1.1*	*0.002*
V1	*0.042 ±0.0008*	*0.042 ±0.0007*	*0.0386*	*0.88*	*0.7*	*0.019*

Results regarding Slow-5 band across 14 subjects comparing conditions (iii) and (ii) are shown in Table 6. Mean power values in the filtered signal remain very similar to the unfiltered, with percentage reductions <2.5%, and with correspondent power loss < 0.08 dB in all VOIs. There is no statistical difference in CC, CRBL ($p > 0.05$), reflected by relatively lower effect size. M1 and SPL have the highest mean power in the unfiltered condition, followed by SMAPMC, CC and CRBL. V1 has the lowest mean power in both conditions. In condition (iii) SPL has the most significant change, reflected by the larger effect size.

Table 7. Slow-4 across 14 subjects in condition iii) Filtered after VOI extraction compared to condition ii) Unfiltered

ROI	*Unfiltered (condition ii) Mean Power ± SD*	*Filtered (condition iii) Mean Power ± SD*	*Mean Power Loss [dB]*	*Mean Power Reduction [%]*	*Effect Size - d*	*p-values*
CC	*0.131±0.002*	*0.131±0.002*	*0.0010*	*0.02*	*0.1*	*0.810*
CRBL	*0.149±0.002*	*0.148±0.002*	*0.0008*	*0.02*	*0.3*	*0.301*
M1	*0.250±0.018*	*0.250±0.018*	*0.0004*	*0.01*	*0.2*	*0.449*
SMAPMC	*0.154±0.002*	*0.153±0.002*	*0.0020*	*0.05*	*0.5*	*0.081*
SPL	*0.208±0.036*	*0.208±0.036*	*0.0008*	*0.02*	*0.1*	*0.780*
V1	*0.109±0.002*	*0.108±0.002*	*0.0008*	*0.02*	*0.3*	*0.269*

Results regarding the Slow-4 band, comparing conditions (iii) and (ii), are shown in (Table 7). Mean power values are nearly identical, with mean power reduction below 0.05% and power loss close to zero. Effect sizes remain small and there a no statistically significant difference among VOIs.

6.5 Fixed Effective Connectivity – DCM (Impact on DCM Analysis)

The five models, described in Methods, were specified and estimated for the different datasets resulting from the three filtering conditions on the subset of 14 subjects. After estimation BMS was performed for each condition on the five models. The results report the PEP for the competing models Figure 33. In the unfiltered condition (Figure 33.a) model 4 shows a prominent probability (~90%), model 1 has ~10% probability, other models (2,3,5) present near zero probabilities. For the filtered condition (Figure 33.b), model 4 remains the most probable, with all other model presenting negligible probabilities. In the filtered after VOI extraction condition (Figure 33.c), PEP is comparable to the unfiltered case for all models, with model 4 having the highest probability (>90%). Across all preprocessing conditions, RFX-BMS identified model 4 as the most likely model.

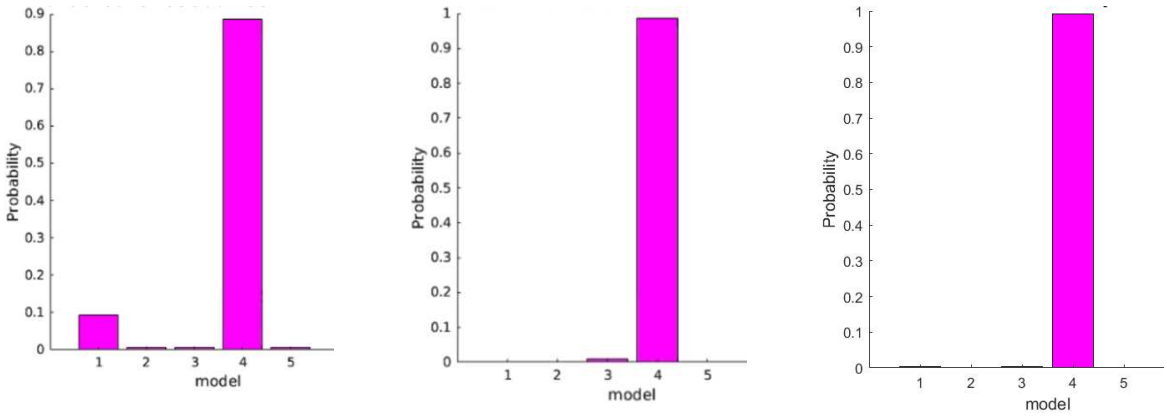

a. Unfiltered (ii) b. Filtered (i) c. Filtered (iii)

Figure 33. Random effects Bayesian Model selection (RFX-BMS) with protected exceedance probabilities (PEP) computed for filtering conditions a) Unfiltered (ii) b) Filtered Before VOI extraction (i) c) Filtered After VOI extraction (iii), identifying Model 4 as the winning model across the 5 models tested.

The group level fixed effective connectivity strength (Hz), estimated through BMA across 14 subjects for the three preprocessing conditions, is shown in the heatmaps (Figure 34). Positive and negative values in the heatmaps represent respectively excitatory (red) and inhibitory (blue) connections for each pair of regions, with self-connection on the diagonal. Across all preprocessing conditions, the overall connectivity is mostly persevered, with consistency in sign and strength of connections. In all three conditions it can be observed that all self-connections are inhibitory, and that stronger excitatory connections occur from V1 to motor areas involved in both planning (CRBL and SMAPMC) and execution (M1). In both cases when filtering was applied (Figure 34.b-c), and especially in the filtered after VOI

extraction condition (Figure 34.c), connections from V1 show an increase in self-inhibition and in excitatory strength towards M1 and CRBL. Similarly, there is an increase in the excitatory connections from M1 to SPL and from SMAPMC to CC. With respect to the unfiltered, there is a decrease in the excitatory connections from SMAPMC to M1. Changes in sign all involve the CRBL. Connection from M1 to CRBL become inhibitory when filtering is applied before and after VOI extraction. In the before VOI extraction filtering condition (Figure 34.b), connection from CRBL to SMAPMC becomes excitatory, while it remains inhibitory in condition after (iii). In condition (iii), connections from CRBL to M1 becomes inhibitory, while it remains positive in condition (i).

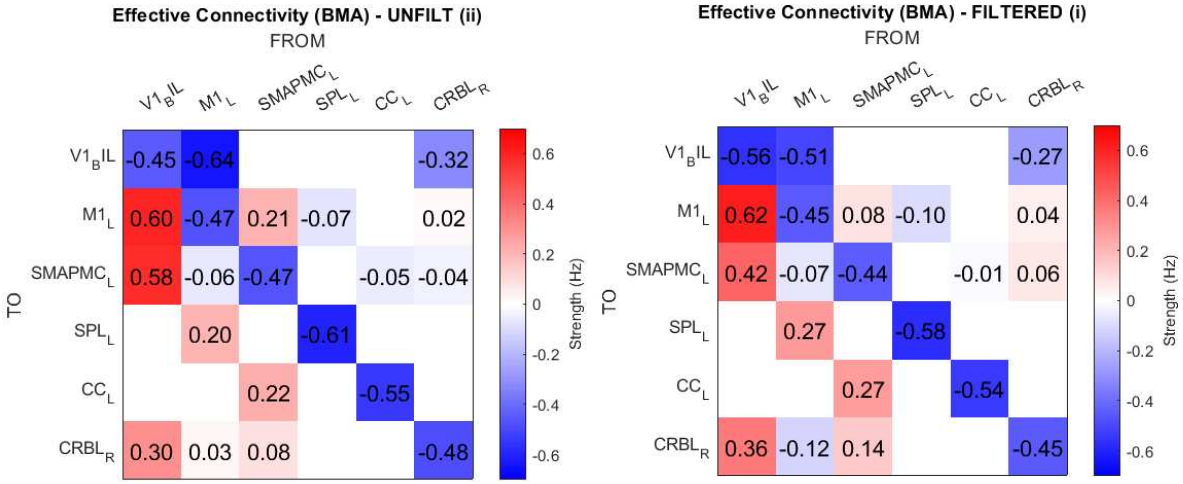

Figure 34. Fixed effective connectivity of winning Model 4 estimated with BMA over 14 subjects, in three preprocessing conditions a) Unfiltered b) Filter applied before VOI extraction c) Filter applied after VOI extraction. Effective connectivity strength expressed in Hz, with positive values for excitatory connections (red), negative values for inhibitory connections (blue), extrinsic connections not included in the model (white). VOIs: V1 - bilateral primary visual cortex, M1 - left primary motor cortex, CRBL - right cerebellum, SMAPMC - left supplementary motor and premotor cortex, CC - left cingulate cortex, SPL - left superior parietal lobule. The acronym of each region reports also the laterality left (L), right (R), bilateral (RL).

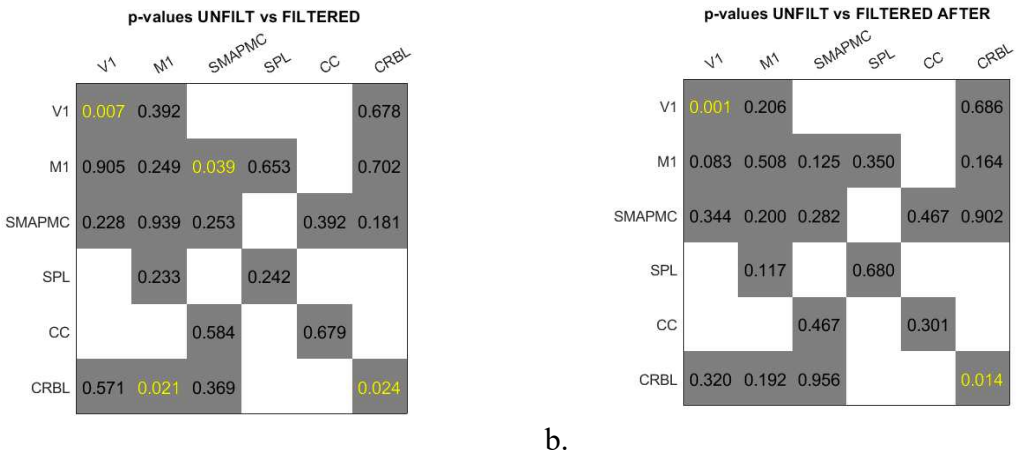

Figure 35. p-values resulting from the pairwise t-test between a) Unfiltered (ii) vs Filtered before VOI extraction (n i) b) Unfiltered (ii) vs filtered after VOI extraction (iii) (yellow are p-values <0.05).

Pairwise t-tests were performed comparing unfiltered condition (ii) to the filtered condition (i) and (iii) respectively. Resulting p-values are shown in Figure 35. From the comparison between (ii) and (i) (Figure 35.a) significant p-values ($p < 0.05$), were observed for V1 and CRBL self-connections and connection from SMAPMC and M1 (change in strength, Figure 34.a-b) and from M1 to CRBL (change in sign, Figure 34.a-b). When compared to the filtered after VOI extraction condition (iii) (Figure 35.b), significant differences were detected in V1 and CRBL self-connections ($p<0.05$).

7. Discussion

The main aim of this study was to investigate the effects of the bandpass (0.008 – 0.09 Hz) temporal filtering on the BOLD signal within the DCM framework. Three filtering conditions were defined and compared to assess the implications on the estimation of effective connectivity within the studied visuomotor network. Overall, the results show that filtering significantly affects the spectral characteristics of the BOLD signal but has a limited impact on the effective connectivity estimates.

The choice of the bandpass frequency range is motivated by the spectral characteristics of the BOLD signal which predominantly lies in the 0.01-0.1 Hz range (Chapter 2.4.1). This range comprises both Slow-5 and Slow-4 components and therefore is expected to preserve physiologically meaningful oscillations within these bands, while attenuating frequency components containing respiratory and aliased cardiac signals, such as Slow-3. The applied

filter, described in Chapter 5.4 of Materials and Methods, introduces certain limitations. Signal distortions such as ringing, spectral leakage and attenuation, may be introduced, particularly near the edges of the passband (Oppenheim & Schafer, 1999). Thus, frequency components close to the cut off frequencies, such as those in the Slow-5 band and Slow-3 bands, are particularly susceptible to these artifacts due to the abrupt transition of the filter.

Giving this expectation, synthetic signals were first used to provide a controlled reference for better understanding the effects of the filtering procedure on known spectral components positioned within the Slow bands. For X1 and X2 synthetic signals, the application of the ideal bandpass filter, preserved the overall temporal structure and reduced the higher frequency oscillations. In the frequency domain, components outside the passband were effectively suppressed, while those within the band were affected depending on their proximity to the cut off frequencies. Components near transition bands showed a more prominent attenuation, while the components within Slow-4 were less affected. Overall, these findings indicate that the bandpass filter does not behave as an ideal frequency selector, but introduces attenuation even within the passband, particularly for components close to the cut off frequencies.

Once applied to real BOLD signals, these filtering effects can influence the physiological interpretation of the signal, as slow-frequency components carry meaningful information. For example, Slow-3 mostly out of the passband, has been associated with local neural processes, and an artificial attenuation introduced by the filter can affect the neurophysiological interpretation of advanced analysis such as the effective connectivity ones. For this reason, once the filter behaviour is established on a synthetic signal, its application to real data is fundamental for understanding the potential bias introduced by the signal preprocessing. In the real BOLD data, filter application before and after VOI extraction mostly suppressed the Slow-3 band and reduced the signal amplitude within the passband, with a stronger effect on the Slow-5, as it is closer the inferior cut off.

An important aspect emerging from the results concerns the impact of filtering on the VOI extraction procedure itself. The observed reduction in signal amplitude, when filtering is applied before VOI extraction, does not only affect spectral properties of the signal but also influences the statistical significance of regional activations, resulting in missing regions in

7 subjects. This effect is particularly relevant for regions such as V1 and CRBL where a greater variability in power distribution across subjects was observed from the PSD analysis. The unfiltered data indeed had a successful VOI extraction for all 21 subjects. This highlights that filtering applied before VOI extraction impacts the definition of the network itself, introducing a limitation in the connectivity analyses due to missing regions and reduced sample size. For comparability across filtering conditions, the original sample of 21 subjects was reduced to 14 subjects with complete VOI extraction.

Filtering applied after the complete VOI extraction of 14 subjects, preserved the spectral content more effectively with a minimal but systematic power attenuation of power across regions. Spectral attenuation resulted statistically significant, this reflects the systematic effect of the filter rather than the magnitude of the power loss.

The stronger attenuation observed when filtering is applied before VOI extraction may be explained by the voxel-wise application of the filter, which influences not only spectral and temporal signal characteristics but also its statistical properties. Filtering leads to a decrease in variance and signal amplitude reducing contrast between task and baseline. Filtering also leads an increase in autocorrelation of voxel-wise timeseries, reducing the number of effectively independent observations (i.e., degrees of freedom) (Davey et al., 2013). Overall, this affects the GLM analysis leading to lower β estimates and lower t-statistics (i.,e., lower SPM{T} maps Figure 22 - Figure 23), which show reduced activation intensity. Therefore, fewer voxels reach the statistical significance threshold resulting in incomplete VOI extraction, coherently with what was observed in Results (Chapters 6.2-6.3). Furthermore, VOI times series are extracted as the first eigenvariate within each region, which depends on the variance across voxels, thus the resulting representative time series is again affected by the filtering operation. Moreover, there might be interactions between filtering procedures and nuisance regression procedures in the real BOLD data, which also may result in signal attenuation

Despite the differences at signal level, BMS identified Model 4 (Figure 20.4) as the most likely model for all three conditions. This indicates that the underlying model structure is robust to the different filtering strategies and represents the most likely hypothesis on the network interconnections. The group-level fixed effective connectivity estimated through

BMA also shows stability in the pattern of connections, as the sign and strength of most connections remains consistent. The winning model highlights the hypothesis of a visual-to-plan and execution functional loop, as V1 is connected to motor planning areas (CRBL and SMAPMC) and motor execution (M1). This organization is consistent with the visuomotor nature of the task, where the visual information is processed and then transformed in motor commands after planning. Temporal filtering did not alter the overall connectivity; however, it appears to modulate the relative strength in planning and execution pathways. Particularly, in the filtered conditions, there is an increase in the excitatory strength of connections departing from V1 to CRBL and M1. Internal motor planning connections, such those from SMAPMC and M1 showed a reduction in the connection's strength, while connection from M1 to CRBL changed from excitatory to inhibitory. This might suggest that filtering may increase the relative contribution of visually driven connections, resulting in more enhanced visuo-to-plan pathways, while slightly reducing internal motor connections. This effect can be interpreted given the spectral changes observed in the BOLD signal. As the quantitative analysis showed stronger attenuation in the Slow-5 band, which is associated with larger scale integrative processes. This may explain the reduction in the influence of planning regions. While the preservation of Slow-4, more closely associated with task related dynamics, may contribute to the strengthening of visually driven connections. Different Slow-4 and Slow-5 attenuations might also explain variations in CRBL as it may rely on a combination of these frequency components. Also, it is interestingly noted that when filtering is applied after VOI extraction, the spectral content within both Slow-5 and Slow-4 are better preserved, compared to the before VOI extraction filter application. This is reflected in the connectivity results, which remain more like the unfiltered condition.

While this study provides the evaluation of the filtering role on BOLD signal properties and its impact on effective connectivity estimation with DCM, there are limitations regarding this study to be considered. The analysis was restricted to 14 subjects for which VOI extraction was completed. Although this ensured consistency for the comparison the sample size is reduced, thus limiting the generalizability of the results. The analysis focused on the use of a single filter type, and these results are not generalizable for other filtering approaches. The

analysis focused exclusively on the fixed effective connectivity without including the modulatory effects, therefore the study does not include task dependent modulations.

Future work could address these limitations by including larger cohorts, investigate different filter designs and incorporating modulatory effects in DCM. To better understand the extent to which filtering impacts DCM analyses, different filter designs and interaction with other preprocessing steps may provide a further insight on how preprocessing choices propagate through the DCM pipeline. In addition, further attention should be given to the functional role of slow-frequency bands, whose specific contribution to neural processes is still not fully understood.

8. Conclusion

This thesis focused on the study of the role of temporal filtering on BOLD signal properties and on estimation of fixed effective connectivity within the visuomotor network. This highlighted also how filter application and order of application influence different stages of the DCM pipeline. Results demonstrated that filtering induces a significant signal change in both cases when filtering was applied with respect to the unfiltered signal, with filtering after VOI extraction condition being more conservative of the passband power. In the DCM analysis filtering was found to have limited modulation effects on the connection. Finally, these observations highlight that the impact of the bandpass filter applied is not uniform across the pipeline, as earlier steps of GLM and VOI extraction are more sensitive to filtering while connectivity estimation is more stable. From a methodological perspective, this might suggest that the post-VOI extraction filtering strategy is more reliable, as it better preserves in-band spectral characteristics while still attenuating higher frequency components. In conclusion, this work emphasizes that temporal filtering can influence not only signal characteristics but also the interpretation of functional brain dynamics and should be considered within the design of fMRI preprocessing pipelines. Therefore, filtering procedures have a role in reproducibility of the studies, as they affect results and their interpretability.

References

Alahmadi, A. A. S., Samson, R. S., Gasston, D., Pardini, M., Friston, K. J., D'Angelo, E., Toosy, A. T., & Wheeler-Kingshott, C. A. M. (2016). Complex motor task associated with non-linear BOLD responses in cerebro-cortical areas and cerebellum. *Brain Structure and Function*, *221*(5), 2443–2458. https://doi.org/10.1007/s00429-015-1048-1

Alan V. Oppenheim, & Ronald W. Schafer. (1999). *Discrete Time Signal Processing Second Edition*. 55–60, 542, 703.

Bandettini, P. A. (2012). Twenty years of functional MRI: The science and the stories. In *NeuroImage* (Vol. 62, Number 2, pp. 575–588). https://doi.org/10.1016/j.neuroimage.2012.04.026

Brown, R. W. ., Cheng, Y.-C. N. ., Haacke, E. Mark., Thompson, M. R. ., & Venkatesan, Ramesh. (2014). *Magnetic resonance imaging : physical principles and sequence design*. John Wiley & Sons, Inc.

Brydges, C. R. (2019). Effect Size Guidelines, Sample Size Calculations, and Statistical Power in Gerontology. *Innovation in Aging*, *3*(4). https://doi.org/10.1093/geroni/igz036

Casey, B. J., Davidson, M., & Rosen, B. (2002). Functional magnetic resonance imaging: basic principles of and application to developmental science. In *Developmental Science* (Vol. 5).

Casiraghi, L., Alahmadi, A. A. S., Monteverdi, A., Palesi, F., Castellazzi, G., Savini, G., Friston, K., Gandini Wheeler-Kingshott, C. A. M., & D'Angelo, E. (2019). I see your effort: Force-Related BOLD effects in an extended action execution-observation network involving the cerebellum. *Cerebral Cortex*, *29*(3), 1351–1368. https://doi.org/10.1093/cercor/bhy322

Chao-Gan, Y., & Yu-Feng, Z. (2010). DPARSF: A MATLAB toolbox for "pipeline" data analysis of resting-state fMRI. *Frontiers in Systems Neuroscience*, *4*. https://doi.org/10.3389/fnsys.2010.00013

Chen, G., Taylor, P. A., Reynolds, R. C., Leibenluft, E., Pine, D. S., Brotman, M. A., Pagliaccio, D., & Haller, S. P. (2023a). BOLD Response is more than just magnitude: Improving detection sensitivity through capturing hemodynamic profiles. *NeuroImage*, *277*. https://doi.org/10.1016/j.neuroimage.2023.120224

Chen, G., Taylor, P. A., Reynolds, R. C., Leibenluft, E., Pine, D. S., Brotman, M. A., Pagliaccio, D., & Haller, S. P. (2023b). *BOLD response is more than just magnitude:*

improving detection sensitivity through capturing hemodynamic profiles. https://doi.org/10.1101/2023.02.13.528362

Chen, J. E., & Glover, G. H. (2015). BOLD fractional contribution to resting-state functional connectivity above 0.1Hz. *NeuroImage*, *107*, 207–218. https://doi.org/10.1016/j.neuroimage.2014.12.012

Cheng, Y. N., & Haacke, E. M. (2001). Fundamental Properties of Magnetization. *Current Protocols in Magnetic Resonance Imaging*, *1*(1). https://doi.org/10.1002/0471142719.mib0103s01

Cohen, J. (1988). *Statistical Power Analysis for the Behavioral Sciences Second Edition*.

Cordes, D., Haughton, V. M., Arfanakis, K., Carew, J. D., Turski, P. A., Moritz, C. H., Quigley, M. A., & Meyerand, M. E. (2001). Frequencies Contributing to Functional Connectivity in the Cerebral Cortex in "'Resting-state'" Data. In *AJNR Am J Neuroradiol* (Vol. 22).

Davey, C. E., Grayden, D. B., Egan, G. F., & Johnston, L. A. (2013). Filtering induces correlation in fMRI resting state data. *NeuroImage*, *64*(1), 728–740. https://doi.org/10.1016/j.neuroimage.2012.08.022

Felician, O., Romaiguère, P., Anton, J. L., Nazarian, B., Roth, M., Poncet, M., & Roll, J. P. (2004). The Role of Human Left Superior Parietal Lobule in Body Part Localization. *Annals of Neurology*, *55*(5), 749–751. https://doi.org/10.1002/ana.20109

Friston, K., Holmes, A., Worsley, K., Poline, J., Frith, C., & Frackowiak, R. (1995). Statistical Parametric Maps in Functional Imaging: A General Linear Approach. In + *Human Brain Mapping* (Vol. 2).

Friston, K. J., Harrison, L., & Penny, W. (2003). Dynamic causal modelling. *NeuroImage*, *19*(4), 1273–1302. https://doi.org/10.1016/S1053-8119(03)00202-7

Glover, G. H. (2011). Overview of functional magnetic resonance imaging. In *Neurosurgery Clinics of North America* (Vol. 22, Number 2, pp. 133–139). https://doi.org/10.1016/j.nec.2010.11.001

Gregory Ashby, F. (2015). An introduction to fMRI. In *An Introduction to Model-Based Cognitive Neuroscience*. Springer New York. https://doi.org/10.1007/978-1-4939-2236-9_5

Grover, V. P. B., Tognarelli, J. M., Crossey, M. M. E., Cox, I. J., Taylor-Robinson, S. D., & McPhail, M. J. W. (2015). Magnetic Resonance Imaging: Principles and Techniques: Lessons for Clinicians. In *Journal of Clinical and Experimental Hepatology* (Vol. 5, Number 3, pp. 246–255). Elsevier B.V. https://doi.org/10.1016/j.jceh.2015.08.001

Huettel, S. A., Song, A. W., & Mccarthy, G. (2014). *Third Edition FUNCTIONAL Magnetic Resonance Imaging*.

John P. Mugler. (1999). *OVERVIEW OF MR IMAGING PULSE SEQUENCES*. https://doi.org/10.1016/s1064-9689(21)00516-x

Jung, B. A., & Weigel, M. (2013). Spin echo magnetic resonance imaging. In *Journal of Magnetic Resonance Imaging* (Vol. 37, Number 4, pp. 805–817). https://doi.org/10.1002/jmri.24068

Koc, N. A., Rakowski, M., Dębska, A., Szmyd, B., Zawadzka, A., Zaczkowski, K., Podstawka, M., Wilmańska, D., Dobek, A., Stefańczyk, L., Jaskólski, D. J., & Wiśniewski, K. (2026). Theoretical, Technical, and Analytical Foundations of Task-Based and Resting-State Functional Magnetic Resonance Imaging (fMRI)—A Narrative Review. In *Biomedicines* (Vol. 14, Number 2). Multidisciplinary Digital Publishing Institute (MDPI). https://doi.org/10.3390/biomedicines14020333

Lee, T. S., Mumford, D., Romero, R., & Lamme, V. A. F. (1998). The role of the primary visual cortex in higher level vision. In *Vision Research* (Vol. 38).

Lorenzi, R. M., Korkmaz, G., Alahmadi, A. A. S., Monteverdi, A., Casiraghi, L., D'Angelo, E., Palesi, F., & Gandini Wheeler-Kingshott, C. A. M. (2025). Cerebellar control over inter-regional excitatory/inhibitory dynamics discriminates execution from observation of an action. *Cerebellum*, *24*(4). https://doi.org/10.1007/s12311-025-01863-6

Matthews, P. M., & Jezzard P. (2004). Functional magnetic resonance imaging. In *J Neurol Neurosurg Psychiatry* (Vol. 75). www.jnnp.com

Monti, M. M. (2011). Statistical analysis of fMRI time-series: A critical review of the GLM approach. *Frontiers in Human Neuroscience*, (MARCH). https://doi.org/10.3389/fnhum.2011.00028

Moratal, D., Vallés-Luch, A., Martí-Bonmati, L., & Brummers, M. E. (2008). k-Space tutorial: An MRI educational tool for a better understanding of k-space. *Biomedical Imaging and Intervention Journal*, *4*(1). https://doi.org/10.2349/biij.4.1.e15

Plewes, D. B., & Kucharczyk, W. (2012). Physics of MRI: A primer. In *Journal of Magnetic Resonance Imaging* (Vol. 35, Number 5, pp. 1038–1054). https://doi.org/10.1002/jmri.23642

Pooley, R. A. (2005). Fundamental physics of MR imaging. *Radiographics*, *25*(4), 1087–1099. https://doi.org/10.1148/rg.254055027

Prati, J. M., Pontes-Silva, A., & Gianlorenço, A. C. L. (2024). The cerebellum and its connections to other brain structures involved in motor and non-motor functions: A

comprehensive review. In *Behavioural Brain Research* (Vol. 465). Elsevier B.V. https://doi.org/10.1016/j.bbr.2024.114933

Ray H. Hashemi, C. J. L. & W. B. (2018). *MRI: The Basics*. https://www.ebsco.com/terms-of-use.

Ray H. Hashemi, Christopher J. Lisanti, & William Bradley. (2018a). *2 Basic Principles of MRI*. https://www.ebsco.com/terms-of-use.

Ray H. Hashemi, Christopher J. Lisanti, & William Bradley. (2018b). *MRI: The Basics*. https://www.ebsco.com/terms-of-use.

Roland, P. E., Larsen, B., Lassen, N. A., & Skinhoj, E. (1980). Supplementary Motor Area and Other Cortical Areas in Organization of Voluntary Movements in Man. In *JOURNALOF NEUROPHYSIOLOGY* (Vol. 43, Number 1).

Rolls, E. T. (2019). The cingulate cortex and limbic systems for emotion, action, and memory. In *Brain Structure and Function* (Vol. 224, Number 9, pp. 3001–3018). Springer. https://doi.org/10.1007/s00429-019-01945-2

Sanes, J. N., & Donoghue, J. P. (2026). PLASTICITY AND PRIMARY MOTOR CORTEX. In *Annu. Rev. Neurosci* (Vol. 23). www.annualreviews.org.

Sexton, J. A., Deshpande, G., Li, Z., Glielmi, C. B., & Hu, X. P. (2013). Functional Magnetic Resonance Imaging. In *Neural Engineering* (pp. 473–497). Springer US. https://doi.org/10.1007/978-1-4614-5227-0_11

Smitha, K. A., Akhil Raja, K., Arun, K. M., Rajesh, P. G., Thomas, B., Kapilamoorthy, T. R., & Kesavadas, C. (2017). Resting state fMRI: A review on methods in resting state connectivity analysis and resting state networks. In *Neuroradiology Journal* (Vol. 30, Number 4, pp. 305–317). SAGE Publications Inc. https://doi.org/10.1177/1971400917697342

Stephan, K. E., Penny, W. D., Daunizeau, J., Moran, R. J., & Friston, K. J. (2009). Bayesian model selection for group studies. *NeuroImage*, *46*(4), 1004–1017. https://doi.org/10.1016/j.neuroimage.2009.03.025

Stephan, K. E., Penny, W. D., Moran, R. J., den Ouden, H. E. M., Daunizeau, J., & Friston, K. J. (2010). Ten simple rules for dynamic causal modeling. In *NeuroImage* (Vol. 49, Number 4, pp. 3099–3109). https://doi.org/10.1016/j.neuroimage.2009.11.015

Val M. Runge, Wolfgang R. Nitz, & Johannes Thomas Heverhagen. (2018). *The Physics of Clinical MR Taught Through Images*. https://doi.org/10.1055/b-0038-162958

Van Oostende, S., Van Hecke, P., Sunaert, S., Nuttin, B., & Marchal, G. (1997). *FMRI Studies of the Supplementary Motor Area and the Premotor Cortex*.

Wei, W., Zhang, K., Chang, J., Zhang, S., Ma, L., Wang, H., Zhang, M., Zu, Z., Yang, L., Chen, F., Fan, C., & Li, X. (2024). Analyzing 20 years of Resting-State fMRI Research: Trends and collaborative networks revealed. In *Brain Research* (Vol. 1822). Elsevier B.V. https://doi.org/10.1016/j.brainres.2023.148634

Zeidman, P., Jafarian, A., Corbin, N., Seghier, M. L., Razi, A., Price, C. J., & Friston, K. J. (2019). A guide to group effective connectivity analysis, part 1: First level analysis with DCM for fMRI. *NeuroImage*, *200*, 174–190. https://doi.org/10.1016/j.neuroimage.2019.06.031

Zuo, X. N., Di Martino, A., Kelly, C., Shehzad, Z. E., Gee, D. G., Klein, D. F., Castellanos, F. X., Biswal, B. B., & Milham, M. P. (2010). The oscillating brain: Complex and reliable. *NeuroImage*, *49*(2), 1432–1445. https://doi.org/10.1016/j.neuroimage.2009.09.037